



Unique heterointerface engineering of Ni₂P–MnP nanosheets coupled Co₂P nanoflowers as hierarchical dual-functional electrocatalyst for highly proficient overall water-splitting

Mani Ram Kandel^{a,b}, Uday Narayan Pan^a, Purna Prasad Dhakal^a, Ram Babu Ghising^a, Thanh Tuan Nguyen^a, Junhuan Zhao^c, Nam Hoon Kim^{a,*}, Joong Hee Lee^{a,d,**}

^a Department of Nano Convergence Engineering (BK21 FOUR), Jeonbuk National University, Jeonju, Jeonbuk 54896, Republic of Korea

^b Department of Chemistry, Tribhuvan University, Amrit Campus, Kathmandu 44613 Nepal

^c Zhejiang RUICO Advanced Materials Co Ltd., No. 188 Liangshan Rd, Functional Area, Linghu, Nanxun, Huzhou, Zhejiang, China

^d Carbon Composite Research Centre, Department of Polymer-Nano Science and Technology, Jeonbuk National University, Jeonju, Jeonbuk 54896, Republic of Korea

ARTICLE INFO

Keywords:

Dual-functional electrocatalyst
Hybrid heterostructure
Heterointerface interaction
Phosphidation
Overall water-splitting

ABSTRACT

A noble-metal-free electrocatalyst comprised of hybrid Ni₂P–MnP nanosheet coupled with Co₂P nanoflowers (Ni₂P–MnP@Co₂P) reinforced on nickel foam has been achieved with a unique heterostructure architecture for highly competent hydrogen evolution reaction (HER) and oxygen evolution reaction (OER). Tri-phased Ni₂P–MnP@Co₂P nanocrystal offers tremendously active and robust electrocatalytic efficacy heralded by low HER (60 mV) and OER (255 mV) to achieve (10 and 30) mA cm^{−2} current densities, respectively. The outstanding electrochemical performance is due to the distinctive architectural feature, high surface area with optimum porosity, bountiful Ni₂P–MnP and Co₂P heterointerface interaction, and synergism among Ni₂P, MnP, and Co₂P multi-active sites. The Ni₂P–MnP@Co₂P (+, −) alkaline electrolyzer delivers a low cell voltage of 1.50 V at a current density of 10 mA cm^{−2}, along with astonishing long-term robustness. Moreover, the electrocatalyst displays a Faradaic yield of around (97.2 and 97.9) % at 50 mA cm^{−2} for H₂ and O₂ respectively. This work is expected to pave the way for novel insights into the fabrication of efficient electrocatalysts for practical water-splitting applications.

1. Introduction

Electrochemical water-splitting ($\text{H}_2\text{O} \rightarrow \text{H}_2 + 1/2 \text{O}_2$), an efficient and promising technique to produce carbon-free fuel with high integrity, is practiced as one of the utmost encouraging and viable ways to generate hydrogen and oxygen [1–3]. The overall electrochemical water-splitting proceeds with two vital half-reactions: the hydrogen evolution reaction (HER) as a cathodic two-electron transfer reaction, and the oxygen evolution reaction (OER) as an anodic four-electron transfer reaction [4,5]. However, the sluggish kinetics and multi-proton-electron transfer are the bottlenecks for both HER and OER [6]. Earlier reported research showed that the increased overpotential and electrocatalytic efficiency can be upgraded using more powerful electrocatalysts [7]. The noble metal-based electrocatalysts are used as efficient electrocatalysts due to lower potential, significant activity, and

better durability towards the OER and HER, respectively [8,9]. However, their large-scale implementation is constrained by high-cost, less availability, and limitation to only one half-cell reaction (either HER or OER) [6–8]. Therefore, an efficient and alternative electrocatalyst needs to be synthesized for the rational replacement of noble metal electrocatalysts.

Transitional metal phosphides (TMPs) of the first transition metal series in the periodic table have attractive robust features for HER and OER electrocatalysts, due to their well-adjusted properties, like cost-efficiency, natural abundancy, outstanding electrocatalytic performance, and long-term stability [6,10–13]. TMPs, metal atom and phosphorous atoms are covalently bonded (M–P) to each other where the P atom can accept protons as a base for HER, enabling the formation of peroxide intermediate for OER [13–15]. By virtue of the d-electronic configuration and adequate chemical states of the transition metals,

* Corresponding author.

** Corresponding author at: Department of Nano Convergence Engineering (BK21 FOUR), Jeonbuk National University, Jeonju, Jeonbuk 54896, Republic of Korea
E-mail addresses: nhk@jbnu.ac.kr (N.H. Kim), jhl@jbnu.ac.kr (J.H. Lee).

phosphides are formed in optimum chemical conditions [16]. Jiang et al. investigated Co–P films as a dual-functional electrocatalyst for overall water-splitting, which displayed low potentials of 94 and 345 mV at 10 mA cm⁻² towards both HER and OER, respectively, in alkaline electrolytic medium [17]. In this respect, the TMPs with higher electrical conductivity and the synergistic effect from individual atom or component reveal good electrocatalytic performance for overall water-splitting [6,17,18]. Furthermore, the various reports based on theoretical studies confirmed that the introduction of phosphorus atoms alters the d-band center and Fermi-level of transition metals, which could be a driving factor to enhance the electrocatalytic activity [13,16]. Though, charge separation occurs in M–P for better conductivity, electron significantly impedes electron delocalization in the metals by virtue of the high electronegativity of the P atom in phosphide, offering the reduction of charge-transfer resistance [13,19,20]. Hence, it is crucial to enhance the electrical conductivity and electrocatalytic performance via considerable attempts that offer the boosting of electroactive sites and enhance intrinsic activities. Specifically, the integration of transition metal atoms, like Co, Fe, Mn, Ni, and Nb, on the TMPs electrocatalyst reduces the adsorption free energy of reaction intermediates via modulation of the electronic structures and hastening of the kinetics of the reaction [15,21,22]. For instance, the reported multi-metallic NiCoFeP electrocatalyst showed lower potentials of 131 and 273 mV for HER and OER, respectively, compared to the pure NiFeP and CoFeP, due to the reorganization of the electronic structure of Fe, Co, and Ni [15]. In addition, the synthesis of nanostructured phosphide is reported as a better strategy to expand the electrocatalytic activities of overall water-splitting [23]. Electrocatalysts are usually synthesized using solid–gas interaction via a multi-step process that includes low-temperature phosphidation through in situ liberated phosphine (PH₃) gas from ammonium/sodium hypophosphite (NH₄H₂PO₂ or NaH₂PO₂) decomposition [23,24]. The solid–gas synthesis process avoids the unsafe and time-consuming operation process [24,25]. For e. g. (Ni,Co)₂P NF electrocatalyst displayed a remarkable cell voltage (1.54 V) at low current density (10 mA cm⁻²) for overall water-splitting, signifying the efficient method of solid–gas technique for the synthesis of robust HER and OER catalyst [25]. Alternatively, the electrochemical activities of the electrocatalyst are further improved by designing the multicomponent heterostructure [23,25–27]. Moreover, the heterostructure morphology can regulate electronic structure, as well as enlarge the electrochemically active surface area, resulting in robust electrochemical activities [28,29]. Du et al. obtained nanostructure composed of MoP/Ni₂P, which exhibited remarkable electrocatalytic performance towards the overall water-splitting, due to excess interfacial interaction between MoP and Ni₂P phases [30]. Recently, the synthesis of manganese-based multi-metallic phosphides have been regarded as emerging catalysts for electrochemical water-splitting. For illustration, the reported Ni–Mn–P electrocatalyst displayed low potentials of HER (120 mV) and OER (250 mV) at low current density (10 mA cm⁻²), owing to synergism between nickel and manganese, along with its unique architecture. In addition, the incorporation of manganese along with Ni lowers the free energy of H⁺ adsorption; as well, the formation of *OOH provided a better density of electronic states close to the null Fermi level, thus revealing higher charge allocation rates [23, 31]. To date, different nickel and cobalt-based catalysts have been divulged for electrochemical water-splitting [18,23–26,28,30,32,33]. However, the nickel, manganese, and cobalt-based hybrid trimetallic nano-heterostructure of Ni₂P, MnP, and Co₂P has not yet been developed for overall water-splitting. In this regard, the trimetallic nano-heterostructure of Ni₂P, MnP, and Co₂P with higher electrical conductivity and synergism among the Ni, Mn, and Co phosphides holds the potential for superior electrocatalytic performance for overall water-splitting.

Herein, the hybrid Ni₂P–MnP nanosheets coupled with Co₂P nano-flowers supported on nickel foam (Ni₂P–MnP@Co₂P @ NF) is synthesized. For the fabrication of Ni₂P–MnP@Co₂P @ NF, the desired layered

double hydroxide (LDH, i.e., NiMn–LDH@Co–LDH) was first prepared, followed by phosphidation using a controlled CVD technique. The hybrid Ni₂P–MnP@Co₂P heterostructure is used as a dual-functional electrocatalyst for low potential electrochemical water-splitting. The presence of multi-components (Ni₂P, MnP, and Co₂P), and heterointerface interaction between Ni₂P–MnP and Co₂P, offer a strong synergistic effect, which is differentiated from the single Ni₂P, MnP, or Co₂P electrode. The homogeneously grown active Ni₂P–MnP@Co₂P on the conductive 3D-nickel foam empowers the electrolytic conductivity. Additionally, the integration of Ni and Mn in NiMn–phosphide, combining the effect of different phases and charge redistribution, can be accomplished to promote the charge transport, which helps to expand the electrochemical performance and stability of the Ni₂P–MnP@Co₂P heterostructure. The incorporation of Co₂P further accelerates the alteration of electronic structure of active sites on Ni₂P–MnP nanostructure as estimated in the physicochemical properties, due to the effective electronic interaction within the interfaces. Moreover, the density functional theory (DFT) calculations demonstrate that the strong heterointerface interaction among different phases lowers the free energy of H⁺ adsorption and the formation of *OOH provided a better density of electronic states close to the null Fermi level, thus revealing higher charge allocation rates. As anticipated, the Ni₂P–MnP@Co₂P exhibits outstanding HER and OER activities, along with remarkable stability. Thus, the robust, efficient, and binder-free design of Ni₂P–MnP@Co₂P is a novel alternative to establishing a practically usable material with unique design offering vigorous performance for low-potential electrochemical water-splitting.

2. Experimental section

2.1. Chemicals

Nickel foam was provided by Taiyuan Liyuan Lithium Technology Co. Ltd., China. Cobalt (II) nitrate hexahydrate (Co(NO₃)₂·6H₂O; ≥ 98.0 wt%), Manganese nitrate tetrahydrate (Mn(NO₃)₂·4H₂O; ≥ 99.9 wt%), Nickel (II) nitrate hexahydrate (Ni(NO₃)₂·6H₂O; ≥ 99.9 wt%), potassium hydroxide (KOH, ACS reagent; ≥ 85.0 wt%), ammonium fluoride (NH₄F; 99.0 ≥ wt%), urea (NH₂CONH₂; ≥ 99.0 wt%), sodium hypophosphite monohydrate (NaH₂PO₂·H₂O; ≥ 99.9 wt%), catalyst, Pt/C (10 wt% loading), ruthenium (IV) oxide (RuO₂; ≥ 99.9 wt%) commercial Nafion solution (≥ 5 wt%) were provided by Sigma–Aldrich Co. (USA). Acetone (CH₃COCH₃; ≥ 98.0 wt%), ethanol (C₂H₅OH, ≥ 99.9 wt %), and methanol (CH₃OH, ≥ 99.9 wt%) were obtained from Samchun Pure Chemical Co., Ltd. (Korea).

2.2. Synthesis of the hybrid nickel phosphide-manganese phosphide@cobalt phosphide heterostructure supported on nickel foam (Ni₂P–MnP@Co₂P)

To fabricate the NiMn–LDH, Ni(NO₃)₂·6 H₂O (1 mmol), Mn(NO₃)₂·4 H₂O (1 mmol), NH₂CONH₂ (3 mmol), and NH₄F (1.5 mmol) were dissolved in deionized (DI) water (55 mL), to form a homogenous solution. Then, it was transferred to the Teflon-lined autoclave (100 mL), and the pre-cleaned nickel foam (2 cm × 5 cm) was immersed into it, followed by heating at 150 °C for 14 h in an electric oven. After cooling, the material-loaded nickel foam was sequentially splashed with water, followed by ethanol, and finally dried in vacuum oven at 65 °C for 5 h. The NiMn–LDH precursor was transformed to the corresponding NiMn–LDH @Co–LDH via the same facile hydrothermal method as mentioned above, except the use of Co(NO₃)₂·6 H₂O (1.0 mmol), keeping the constant amount of NH₂CONH₂ and NH₄F. The NiMn–LDH precursor was immersed in the solution and heated at 120 °C for 5 h in electric oven. Finally, the NiMn–LDH@Co–LDH precursor was achieved, and dried in vacuum oven at 65 °C for 5 h.

The as-prepared NiMn–LDH@Co–LDH was transformed into the corresponding Ni₂P – MnP@Co₂P using the control chemical vapor

deposition (CVD) technique. In detail, the NiMn-LDH@Co-LDH precursor and $\text{NaH}_2\text{PO}_4 \cdot \text{H}_2\text{O}$ (1.0 mmol) were kept in two porcelain boats, while maintaining the lower stream site for NiMn-LDH@Co-LDH precursor, and the upstream site for the $\text{NaH}_2\text{PO}_4 \cdot \text{H}_2\text{O}$ inside of the quartz tube. Then, the system was run at 375°C for 160 min at a heating rate of 3°C min^{-1} in the presence of continuous argon atmosphere at a rate of 100 sccm.

For comparison, nickel phosphide@cobalt phosphide ($\text{Ni}_2\text{P} @ \text{Co}_2\text{P}$), manganese phosphide@cobalt phosphide ($\text{MnP} @ \text{Co}_2\text{P}$), and cobalt phosphide (Co_2P) were synthesized using the same method as followed in the $\text{Ni}_2\text{P-MnP} @ \text{Co}_2\text{P}$ electrode, except for changing some precursors.

2.3. Electrochemical measurements

All the electrochemical characterizations were performed in the CHI660E electrochemical workstation (CH Instruments, Inc., USA). The HER and OER performances were inspected by using a typical three-electrode system using as-synthesized binder-free $\text{Ni}_2\text{P-MnP} @ \text{Co}_2\text{P}$ (1 cm^2) as the working electrode, with an Ag/AgCl electrode and a graphite rod applied as the reference and counter electrodes, respectively. The $\text{Ni}_2\text{P-MnP} @ \text{Co}_2\text{P}$ (+, -) device was fabricated as a two-electrode system using $\text{Ni}_2\text{P-MnP} @ \text{Co}_2\text{P}$ as both the anode and cathode. The nitrogen-saturated KOH (1.0 M) was used as an electrolytic medium for all electrochemical measurements. All the measured potentials were referenced to the reversible hydrogen electrode (RHE) using the equation $E_{(\text{vs. RHE})} = E_{(\text{vs. Ag/AgCl})} + 0.0591 \text{ pH} + E_{\text{Ag/AgCl}}^0$. The linear sweep voltammetry (LSV) measurements were analyzed at a 2 mV^{-1} scan rate, and modified to iR corrected form using the equation $E_{\text{iR-Corrected value}} = E_{(\text{vs. RHE})} - i \times R_s$ (i – current and R_s – equivalent series resistance) [19]. The Tafel slope measurements were made using the equation: $\eta = a + b \log j$ (η – overpotential, j – current density, a – constant, and b – Tafel slope). [10] The electrical double layer capacitance (EDLC) measurements were obtained using the equation $\text{ECSA} = C_{\text{dl}}/C_s$ (C_s – specific capacitance of a flat surface and C_{dl} – double-layer capacitance) [11]. The electrochemical impedance spectroscopy (EIS) measurements were carried out to measure the charge-transfer resistance (R_{ct}) of the materials. The change in potential during long-term stability for HER and OER was analyzed using chronopotentiometry at 50 mA cm^{-2} . The Faradaic efficiency was measured using the equation: Faradaic efficiency (FE) = $N_{\text{measured}}/J.t/nF$ (N_{measured} – the volume of measured H_2 or O_2 gas, t – time consumed for electrolysis (s), J – the current density (mA cm^{-2}), F – Faradaic constant ($96,485 \text{ C mol}^{-1}$), and n – electron transfer number) [26].

3. Results and discussion

3.1. Material synthesis and morphological characterization

The fabrication of the hybrid $\text{Ni}_2\text{P-MnP} @ \text{Co}_2\text{P}$ heterostructure was initiated to the vertical growth of cobalt hydroxide nanosheets on nickel foam (NiMn-LDH) by reacting the corresponding precursors, as stated in the experimental section. Initially, nickel and manganese precursors were ionized to the corresponding Ni^{2+} and Mn^{2+} ions in DI water solution. During the facile hydrothermal process at 150°C , urea was decomposed into ammonia and carbon dioxide. The ammonia was further hydrolyzed at high temperature and pressure to liberate the hydroxide ions slowly in the solution, offering the formation of NiMn-LDH nanosheets supported on nickel foam substrate (NiMn-LDH). Next, the NiMn-LDH@Co-LDH was formed during the second hydrothermal process using Co^{2+} precursor salt and NiMn-LDH [34,35]. NH_4F assists to refine the morphology of the synthesized material. The fluorine (electronegative element) can enhance the metal ion binding energy and results in the formation of LDH on the surface of NF. Noteworthy, NH_2CONH_2 (having organic carbon) and NH_4F facilitate the reaction by making an alkaline reaction mixture of salts, which

direct the morphological tuning of the materials. The carbon and nitrogen are residual elements which do not show any effect on the chemical transformation and reaction in the synthesized material. The residual impurities were then washed away using DI water followed by ethanol several times, which results in the formation of desired NiMn-LDH@Co-LDH as mentioned (Experimental section) operating conditions, purity and concentration of precursor, and methods of fabrication [11,35,36]. In the third step, NiMn-LDH@Co-LDH was chemically converted into the respective phosphide as $\text{Ni}_2\text{P-MnP} @ \text{Co}_2\text{P}$ by CVD process under Ar-atmosphere. In this process, phosphine gas (PH_3) was liberated by the thermal decomposition of $\text{NaH}_2\text{PO}_4 \cdot \text{H}_2\text{O}$ and met the surface of hybrid NiMn-LDH@Co-LDH nanostructure. The Ni^{2+} , Mn^{2+} , and Co^{2+} ions from NiMn-LDH@Co-LDH precursor further interacted with the PH_3 gas to form NiMn-phosphide and Co_2P respectively to form the hybrid $\text{Ni}_2\text{P-MnP} @ \text{Co}_2\text{P}$ heterostructure (Fig. 1s, scheme) [11,23].

The morphological and structural inspection of the fabricated materials, namely $\text{Ni}_2\text{P-MnP} @ \text{Co}_2\text{P}$, NiMn-LDH@Co-LDH, NiMn-LDH, $\text{Ni}_2\text{P} @ \text{Co}_2\text{P}$, $\text{MnP} @ \text{Co}_2\text{P}$, and Co_2P , were observed using Field emission scanning electron microscopy (FESEM). Fig. S1a of the Supporting Information (SI) shows that the nickel foam (NF) exposed a porous and smooth surface that provides larger space to grow the electrocatalyst, with a good channel to release bubbles, and inhibit the drop in electrocatalytic performance [37]. Highly ordered vertically aligned NiMn-LDH nanosheets were developed consistently on the bare surface of NF (Fig. S2b of the SI). After the facile second hydrothermal process, flower-like Co-LDH nanostructures were developed on the surface of NiMn-LDH nanosheets to form NiMn-LDH@Co-LDH (Fig. S1c of the SI). The porous surface of NiMn-LDH nanosheets and Co-LDH nanoflowers after adhering provides appropriate and stable channels to reduce the electrode-electrolyte resistance [11,34,37]. The subsequent field emission scanning electron microscopy with energy dispersive X-Ray spectroscopy (FESEM-EDX) based element mapping reveals the homogeneous dispensation of Ni, Mn, Co, and O elements throughout the NiMn-LDH@Co-LDH materials (Fig. S2 of the SI). Furthermore, transmission electron microscopy energy-dispersive X-ray spectroscopy (TEM-EDX) elemental mapping of NiMn-LDH@Co-LDH displayed the existence of Ni, Mn, Co, and O which is in agreements with FESEM-EDS elemental mapping results (Fig. S3 of the SI). The morphology of the $\text{Ni}_2\text{P-MnP} @ \text{Co}_2\text{P}$ heterostructure showed that the morphology after low-temperature phosphidation was well preserved (Fig. 1a-c). The roughness on the surface of nanostructure could effectively enhance the surface area and porosity of the hybrid $\text{Ni}_2\text{P-MnP} @ \text{Co}_2\text{P}$ heterostructure. Meanwhile, the formation of two different $\text{Ni}_2\text{P-MnP}$ and Co_2P morphologies on the 3D porous conductive nickel foam substrate could provide numerous electrocatalytic active sites, along with a better way to diffuse the reactant and electrolyte, which could be predictable for good electrocatalytic activities over the entire $\text{Ni}_2\text{P-MnP} @ \text{Co}_2\text{P}$ material [26]. The subsequent FESEM-EDX based element mapping reveals the homogeneous dispensation of Ni, Mn, Co, and P elements throughout the materials (Fig. S4 of the SI). Furthermore, the morphology of hybrid $\text{Ni}_2\text{P-MnP} @ \text{Co}_2\text{P}$ heterostructure was compared with the FESEM images of control samples $\text{Ni}_2\text{P} @ \text{Co}_2\text{P}$, $\text{MnP} @ \text{Co}_2\text{P}$, and Co_2P (Fig. S5(a-c) of the SI). The $\text{Ni}_2\text{P} @ \text{Co}_2\text{P}$ showed nanoflakes with a relatively bland type of heterostructure. The $\text{MnP} @ \text{Co}_2\text{P}$ also showed relatively thick and agglomerated nanosheets structure. Similarly, the Co_2P showed uniformly grown nanosheet structure throughout the nickel foam. The observed results suggested a far better morphology of the hybrid $\text{Ni}_2\text{P-MnP} @ \text{Co}_2\text{P}$ heterostructure compared to the control materials. The micro-morphology of the $\text{Ni}_2\text{P-MnP} @ \text{Co}_2\text{P}$ was further confirmed by transmission electron microscopy (TEM) analysis (Fig. 1d). The TEM images showed that the two different morphological structures of $\text{Ni}_2\text{P-MnP}$ nanosheets and Co_2P nanoflower were coupled together to form a hybrid $\text{Ni}_2\text{P-MnP} @ \text{Co}_2\text{P}$ heterostructure, which shows the absolute resemblance to that of the FESEM imagery (Fig. 1a-d). High-resolution transmission electron microscopy (HRTEM)

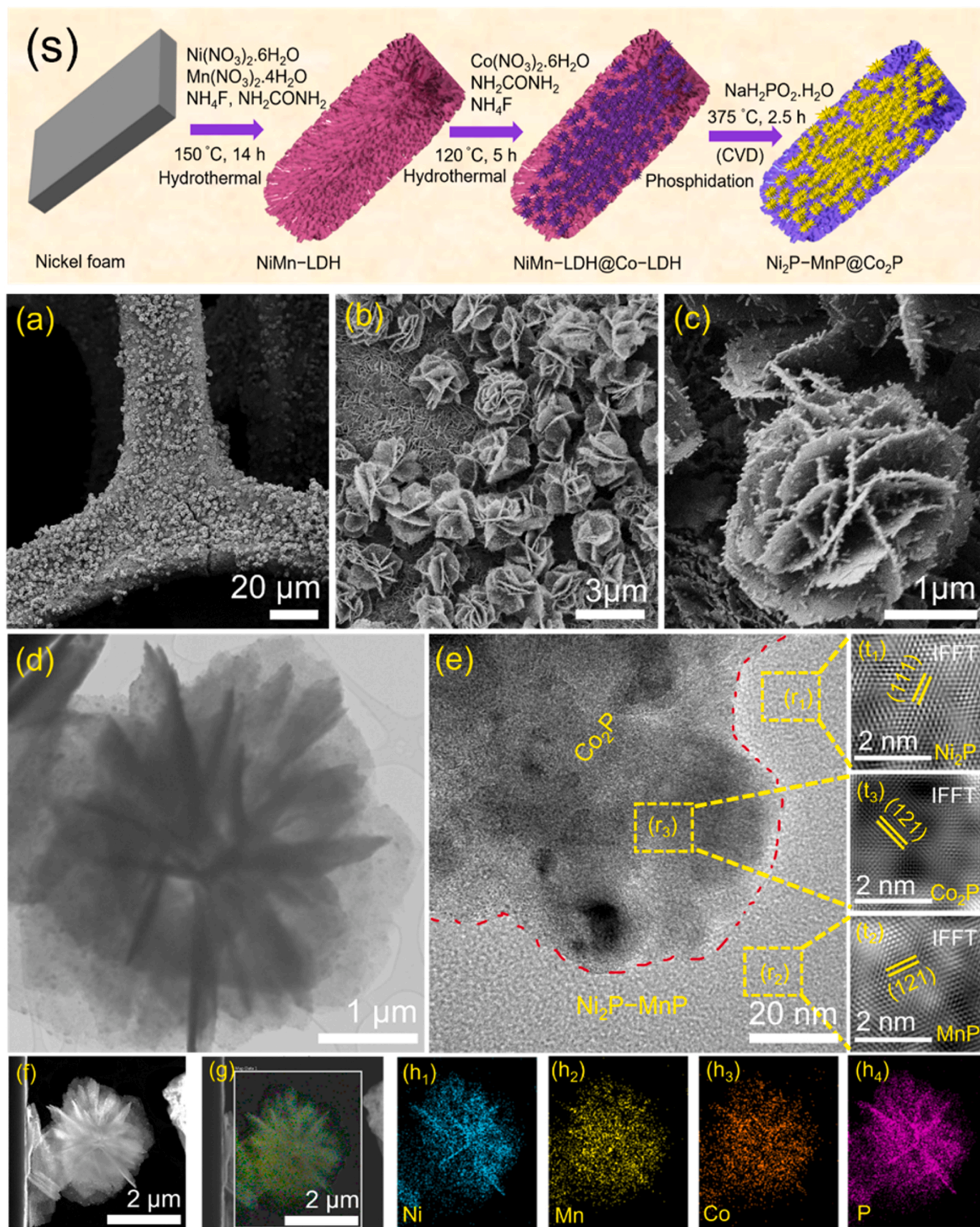


Fig. 1. (s) Schematic of the synthesis of the hybrid $\text{Ni}_2\text{P-MnP@Co}_2\text{P}$ heterostructure. (a)–(c) FESEM images of the $\text{Ni}_2\text{P-MnP@Co}_2\text{P}$ at different magnifications. (d) TEM images of $\text{Ni}_2\text{P-MnP@Co}_2\text{P}$. (e) HRTEM image of $\text{Ni}_2\text{P-MnP@Co}_2\text{P}$ with (r₁), (r₂), and (r₃) demonstrating the HRTEM corresponding to Ni_2P , MnP , and Co_2P phases respectively, while (t₁), (t₂), and (t₃) display the Inverse fast Fourier transform (IFFT) corresponding to the region (r₁), (r₂), and (r₂), respectively. (f) and (g) The STEM image and merged STEM image, and (h₁)–(h₄) corresponding EDS mapping of $\text{Ni}_2\text{P-MnP@Co}_2\text{P}$.

images further divulged the coupling of Ni_2P -MnP and Co_2P lattice fringes, while signifying the crystallinity of Ni_2P -MnP@ Co_2P (Fig. 1e). Inverse fast Fourier transform images (IFFT) revealed the lattice fringes with precise interplanar spacings of (0.22, 0.19, and 0.22) nm, corresponding to the (111), (121), and (121) lattice planes of Ni_2P , MnP, and Co_2P respectively (Fig. 1t₁-t₃) [23,38]. Thus, the detected lattice planes confirm the presence of Ni_2P , MnP, and Co_2P phases, suggesting the formation of the hybrid Ni_2P -MnP@ Co_2P .

The coupling of Ni_2P -MnP and Co_2P nanostructures may enhance the adsorption potential of the entire Ni_2P -MnP@ Co_2P material for reaction intermediates, which could be expected to provide better performance toward both the HER and OER [26]. Moreover, the scanning transmission electron microscopy (STEM) images (Fig. 1f and g), and respective TEM-EDX color mapping confirm the existence of the elements Ni, Mn, Co, and P in the hybrid Ni_2P -MnP@ Co_2P heterostructure (Fig. 1h₁-h₄). From these observations, it is confirmed that the hybrid Ni_2P -MnP@ Co_2P heterostructure was synthesized successfully.

3.2. Surface area, crystal phase, and surface composition characterization

The higher surface area is associated with more active sites and better porosity, which imply the superiority of the morphology of the electrocatalyst. The surface area of the Ni_2P -MnP@ Co_2P and control samples was evaluated using Brunauer–Emmett–Teller (BET) theory on the N_2 -adsorption–desorption isotherm at 77 K. Additionally, the pore size distribution of the materials was analyzed using the Barrett–Joyner–Halenda (BJH) method. The N_2 adsorption–desorption isotherm of the materials showed the type-IV isotherms (Fig. 2a, and Fig. S6 of the SI) with the consistent distribution of pores in the mesoporous region. The hybrid Ni_2P -MnP@ Co_2P heterostructure demonstrated the largest surface area of $103 \text{ m}^2 \text{ g}^{-1}$ (Fig. 2a) compared to the control materials, namely Ni_2P @ Co_2P , MnP@ Co_2P , and Co_2P of (77, 53, and $32 \text{ m}^2 \text{ g}^{-1}$, respectively (Fig. S6 of the SI). Correspondingly, the Ni_2P -MnP@ Co_2P exposed a superior pore diameter of mean $\sim 4.25 \text{ nm}$

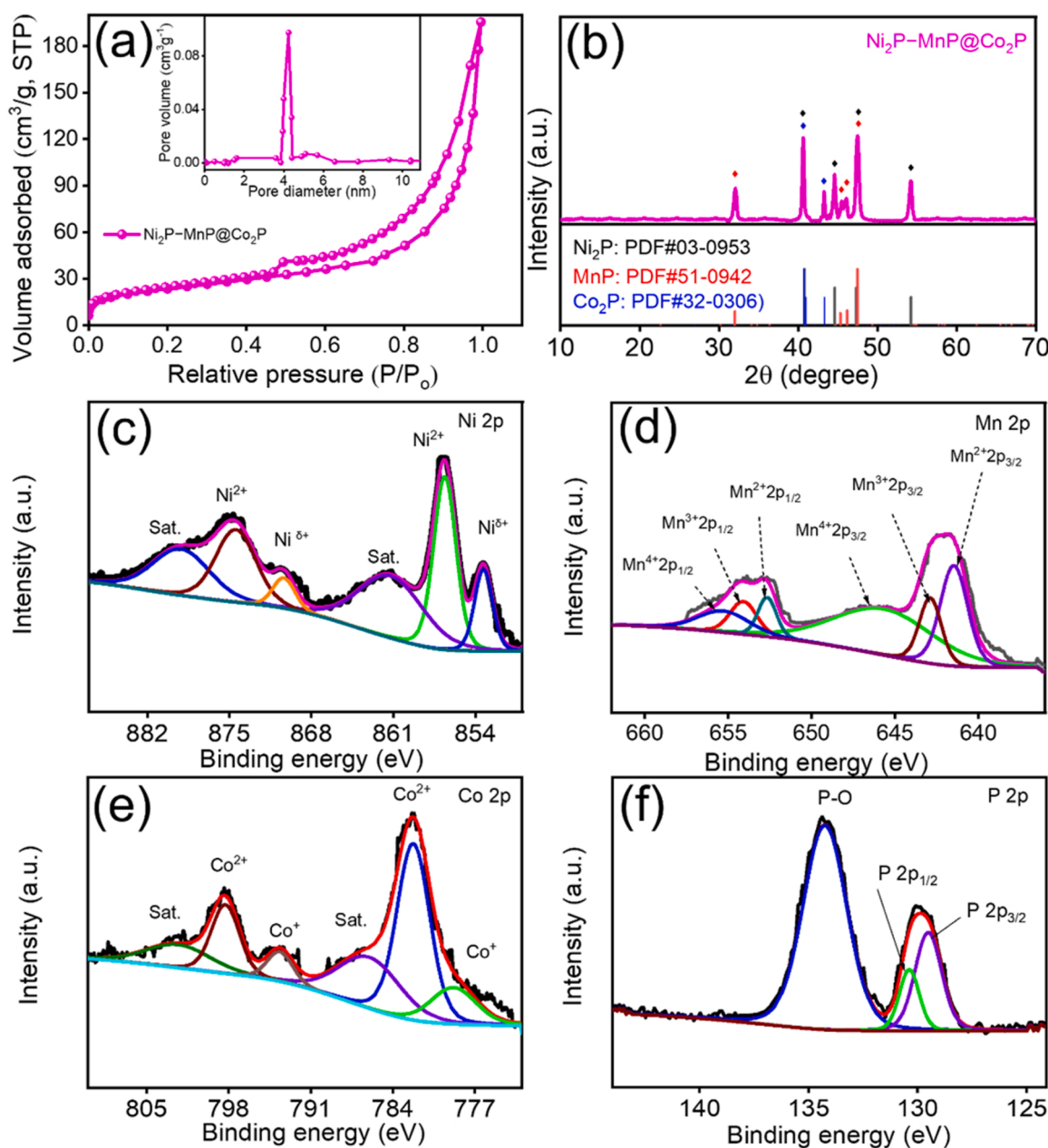


Fig. 2. (a) Nitrogen adsorption–desorption isotherm of the Ni_2P -MnP@ Co_2P (Inset showing the BJH pore size distribution curves of the Ni_2P -MnP@ Co_2P). (b) XRD pattern of the Ni_2P -MnP@ Co_2P . (c)–(f) High-resolution XPS spectra of the Ni 2p, Mn 2p, Co 2p, and P 2p, respectively.

within the range of 0–15 nm (Inset, Fig. 2a), compared to the control materials Ni₂P@Co₂P, MnP@Co₂P, and Co₂P of (3.59, 3.28, and 2.83) nm, respectively, in Fig. S7 of the SI. The proper mesoporous architecture of the Ni₂P–MnP@Co₂P provides an easy way to evolve gaseous bubbles, and prevent the decrease in electrocatalytic performance [28, 39]. The large stress produced by the crystal disparity after the phase transformation from hydroxide to phosphide probably enhances the formation of the numerous tiny nanoparticles in the nanosheets. These nanoparticles are reorganized and aggregated in the form of pores, which accelerate the exposure of additional active sites, possibly enhancing the electrocatalytic performance [40]. Thus, the better mesoporous structure of the Ni₂P–MnP@Co₂P provides manifold active sites, and enables easy penetration of the electrolytic ion into the internal surface of the bulk electrocatalyst, enhancing the electron transportation [41].

The crystal structures of the Ni₂P–MnP@Co₂P and control materials were assessed by X-ray diffraction (XRD) (Fig. 2b, and Fig. S8 of the SI). The XRD pattern of the Ni₂P–MnP@Co₂P was simultaneously consistent

with Ni₂P, MnP, and Co₂P phases (Fig. 2b). The XRD patterns for Ni₂P–MnP@Co₂P were consistent with the diffraction peaks $2\theta = (54.23, 47.3, 44.6, \text{ and } 40.79)^\circ$, corresponding to the (300), (210), (201), and (111) planes, respectively; of Ni₂P (PDF#03–0953), $2\theta = (47.46, 46.18, 45.3, \text{ and } 32.0)^\circ$, corresponding to the (121), (220), (211), and (101) planes, respectively, of MnP (PDF# 51–0942); and $2\theta = (43.29 \text{ and } 40.72)^\circ$, corresponding to the (211) and (121) planes, respectively, of Co₂P (PDF No#32–0306) [23,38]. Only Ni₂P, MnP, and Co₂P diffraction peaks were noticed in the Ni₂P–MnP@Co₂P. The (111), (121), and (121) lattice planes of Ni₂P, MnP, and Co₂P in Fig. 2b are analogous to the lattice planes with the interplanar spacing of (0.22, 0.19, and 0.21) nm, respectively, observed in the HR-TEM and IFFT (Fig. 1t₁–t₃), which confirmed the formation of the pure phased Ni₂P–MnP@Co₂P. For comparison, the XRD patterns of control samples such as Ni₂P@Co₂P, MnP@Co₂P, and Co₂P demonstrated the respective phases (Ni₂P and Co₂P, MnP and Co₂P, and Co₂P), respectively, as presented in Fig. S8 and Table S1 of the SI. The results confirmed that the hybrid Ni₂P–MnP@Co₂P heterostructure was successfully

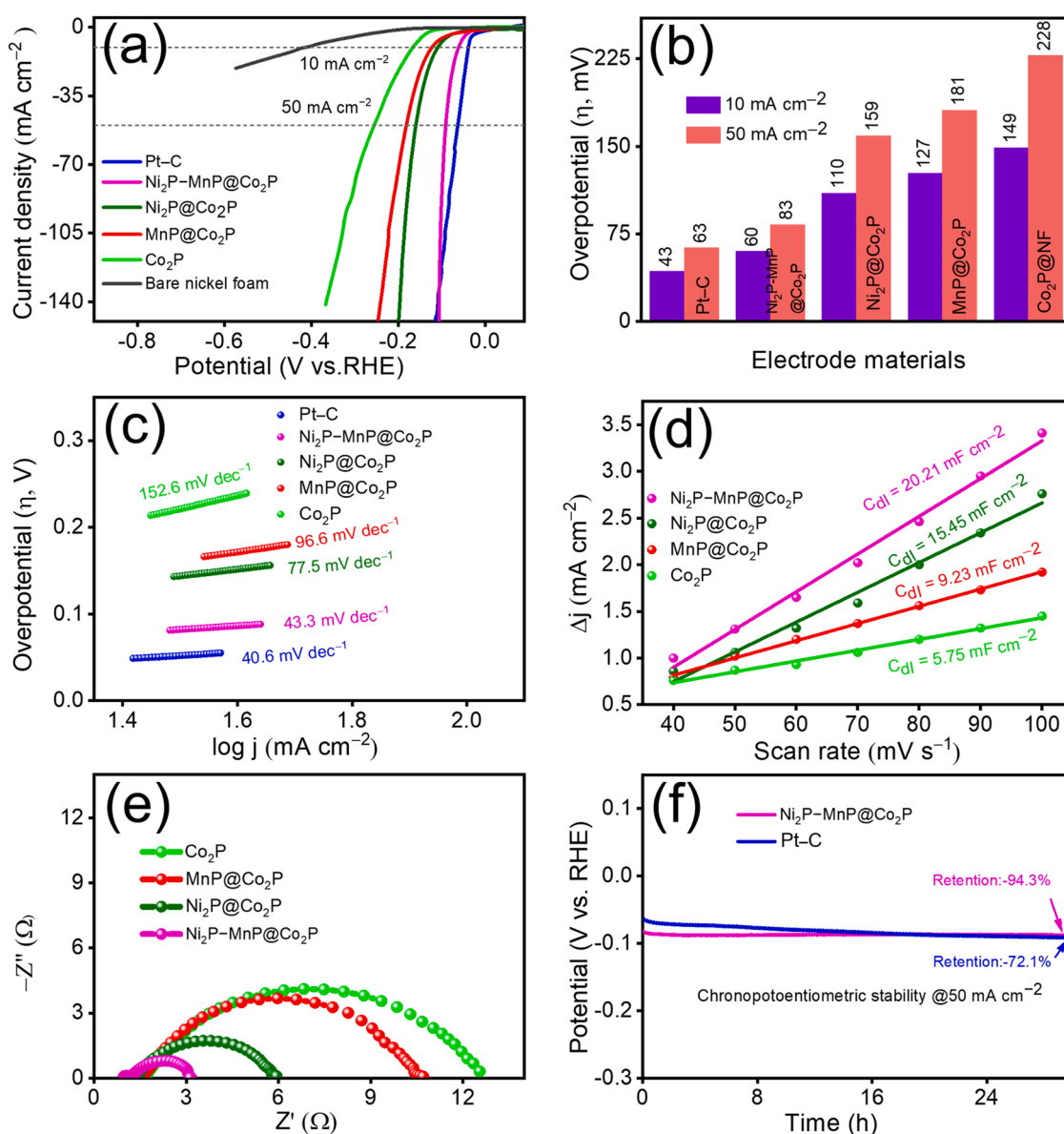


Fig. 3. Electrochemical characterization of HER activity: (a) LSV curves after iR correction of the commercial Pt–C and fabricated samples. (b) Comparative overpotential at (10 and 50) mA cm⁻² of various samples. (c) Tafel plots of different samples. (d) Calculation of C_{dl} using scan rate-dependent current densities for various materials. (e) Nyquist plot for EIS measurements of various materials. (f) Chronopotentiometric curves of Ni₂P–MnP@Co₂P and commercial Pt–C at fixed current density.

engineered.

The surface composition regarding particular electronic states of each constituent element of the hybrid $\text{Ni}_2\text{P}-\text{MnP}@/\text{Co}_2\text{P}$ heterostructure was evaluated via the X-ray photoelectron spectroscopy (XPS) spectrum (Fig. 2c–f). The XPS survey peak of the hybrid $\text{Ni}_2\text{P}-\text{MnP}@/\text{Co}_2\text{P}$ heterostructure (Fig. S9 of the SI) showed the occurrence of Ni, Mn, Co, and P, which was analogous to the results obtained from the energy dispersive X-ray (EDX) color mapping of FE–SEM and TEM (Fig. 1 and Fig. S4 of the SI). However, the insignificant residual C and N peaks observed in the XPS survey spectrum (Fig. S9 of the SI) didn't affect the electrochemical activity of the electrocatalyst due to no additional C and N-based additional C and N containing crystal phases which is in agreements with the HRTEM and XRD analysis [23,42]. The XPS spectra of Ni 2p displayed two peaks at (853.2 and 870.5) eV, corresponding to $\text{Ni}^{\delta+} 2p_{3/2}$ and $\text{Ni}^{\delta+} 2p_{1/2}$, respectively, suggesting the presence of Ni in the form of nickel phosphide (Ni–P). The peak at 853.2 eV that was slightly shifted from the binding energy (852.6 eV) of metallic Ni indicates the presence of $\text{Ni}^{\delta+}$ or Ni^0 species. Two peaks at (856.5 and 874.4) eV correspond to $\text{Ni}^{2+} 2p_{3/2}$ and $\text{Ni}^{2+} 2p_{1/2}$, respectively, suggesting the presence of Ni in the form of phosphate, due to the superficial oxidation of phosphide. Additionally, two peaks centered at (879.6 and 861.2) eV were also detected as satellite peaks (Fig. 3c) [31,40,43,44]. The Mn 2p XPS spectrum exhibited peaks at (641.3 and 652.6) eV for Mn $2p_{3/2}$ and Mn $2p_{1/2}$, respectively, which are equivalent with Mn^{2+} . Meanwhile, the other peaks at (643.1 and 654.0) eV for Mn $2p_{3/2}$ and Mn $2p_{1/2}$, respectively, are corresponded with Mn^{3+} , while peaks at (646.0 and 655.4) eV for Mn $2p_{3/2}$ and Mn $2p_{1/2}$, respectively, are associated with Mn^{4+} (Fig. 3d) [23,31,45]. The XPS spectra of Co 2p showed two peaks at (778.8 and 793.9) eV corresponding to $\text{Co}^+ 2p_{3/2}$ and $\text{Co}^+ 2p_{1/2}$, respectively, suggesting the presence of Co in the form of cobalt phosphide (Co_2P). Two stronger peaks at (782.2 and 798.1) eV correspond to $\text{Co}^{2+} 2p_{3/2}$ and $\text{Co}^{2+} 2p_{1/2}$, respectively, suggesting the presence of Co in the form of CoP . In addition, two satellite peaks at (802.6 and 786.3) eV were also detected (Fig. 3e) [46]. The peaks indicated at (129.2 and 130.3) eV for P $2p_{3/2}$ and P $2p_{1/2}$, respectively, of the P 2p spectrum correspond to the $\text{P}^{\delta-}$ state ($\text{P}^{\delta-}$, $0 < \delta < 1$), suggesting M–P bond in the hybrid $\text{Co}_2\text{P} @ \text{Ni-MnP}@/\text{NF}$ heterostructure [25,47]. The insignificant negative shift in the position of P 2p (129.2 eV) peak from its elemental P 2p (130.0 eV) implied the existence of the $\text{P}^{\delta-}$ state [25,26,47,48]. The peak at 134.2 eV of the P 2p spectrum corresponds to the P–O bond, which is due to surface oxidation (Fig. 3f) [31]. For comparison, we observed the XPS spectrum of $\text{Ni}_2\text{P} @ \text{Co}_2\text{P}$, $\text{MnP}@/\text{Co}_2\text{P}$, and Co_2P (Fig. S10–S11 of the SI). The positive shift of Ni 2p peak and negative shift of Mn 2p peak in the $\text{Ni}_2\text{P}-\text{MnP}@/\text{Co}_2\text{P}$, compared to the pure $\text{Ni}_2\text{P} @ \text{Co}_2\text{P}$ with (852.09 and 856.5) eV for $\text{Ni}^{\delta+} 2p_{3/2}$ and $\text{Ni}^{2+} 2p_{3/2}$, respectively, and $\text{MnP}@/\text{Co}_2\text{P}$ with (641.7, 643.4, and 646.4) eV for Mn^{2+} , Mn^{3+} , and Mn^{4+} , respectively, suggested the strong interaction between Ni_2P and MnP at the heterointerface of $\text{Ni}_2\text{P}-\text{MnP}@/\text{Co}_2\text{P}$ [23,28,32]. The XPS results not only confirm the effective fabrication of hybrid $\text{Ni}_2\text{P}-\text{MnP}@/\text{Co}_2\text{P}$ heterostructure, but also reveal the electron transfer from Ni to Mn by strong $\text{Ni}_2\text{P}-\text{MnP}$ interactions signifying by the positive shifting of Ni 2p binding energy and the negative shifting of Mn 2p binding energy. Hence, the slight fluctuation in the binding energies of the Ni 2p and Mn 2p peaks could suppress the free energies of H^* adsorption and $^*\text{OOH}$ formation, which accelerates the HER and OER performances [23,49].

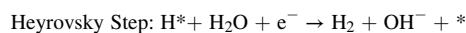
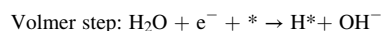
It was noticed that the binding energy of P 2p spectrum in $\text{Ni}_2\text{P}-\text{MnP}@/\text{Co}_2\text{P}$ is positively shifted, compared to the binding energy of P 2p in $\text{Ni}_2\text{P} @ \text{Co}_2\text{P}$, $\text{MnP}@/\text{Co}_2\text{P}$, and Co_2P , demonstrating the strong electronic interaction between metal and phosphorus in the hybrid $\text{Ni}_2\text{P}-\text{MnP}@/\text{Co}_2\text{P}$ heterostructure [32]. The XPS analysis suggests that the hybrid $\text{Ni}_2\text{P}-\text{MnP}@/\text{Co}_2\text{P}$ heterostructure was successfully synthesized.

3.3. Electrochemical characterization

3.3.1. Hydrogen evolution reaction (HER)

The electrocatalytic activities of the hybrid $\text{Ni}_2\text{P}-\text{MnP}@/\text{Co}_2\text{P}$ heterostructure, $\text{Ni}_2\text{P} @ \text{Co}_2\text{P}$, $\text{MnP}@/\text{Co}_2\text{P}$, and Co_2P were probed in 1.0 M KOH solution, using a conventional three-electrode system, in which the as-fabricated materials were used as working electrodes [11]. Electrocatalytic performances of the pure bare nickel foam (NF) and commercial Pt–C were tested for comparison. The linear sweep voltammograms (LSV) polarization curve after iR correction of the hybrid $\text{Ni}_2\text{P}-\text{MnP}@/\text{Co}_2\text{P}$ heterostructure showed better HER performance with overpotential (η) = (60 and 83) mV, compared to other electrode materials, i.e., $\text{Ni}_2\text{P} @ \text{Co}_2\text{P}$, $\text{MnP}@/\text{Co}_2\text{P}$, and Co_2P of (110 and 159, 127 and 180, and 149 and 228) mV at current densities of (10 and 50) mA cm^{-2} respectively (Fig. 3a and b). In contrast, the bare nickel foam did not exhibit noticeable HER performance, which is negligible, as compared to that of the as-synthesized electrode materials. In addition, the overpotential of hybrid $\text{Ni}_2\text{P}-\text{MnP}@/\text{Co}_2\text{P}$ heterostructure is quite near to that of Pt–C catalyst (43 mV), and lower than those of the recently fabricated HER-based electrocatalysts (Table S2 of the SI). As reported in literatures, Pt–C catalyst demonstrates different HER overpotentials due to some operating conditions and the purity of the materials. Specifically, it depends on the amount of precursor, temperature and concentration of the electrolytic solution, and drop-cast volume of the material [50,51]. Furthermore, the purity and methods of synthesis of electrode materials also affect the HER performance of the Pt–C electrocatalyst [52]. In the same way, the synthesized benchmark Pt–C showed the anticipated similarity to the reported literatures (Table S3) [53–56]. Therefore, the better HER performance of the hybrid $\text{Ni}_2\text{P}-\text{MnP}@/\text{Co}_2\text{P}$ heterostructure can be ascribed to the effective hetero-interfacial interaction of the Ni_2P , MnP , and Co_2P phases, as well as the synergism of multiple active sites [23,25,26,28,30]. Furthermore, the HER kinetic activities of the materials were studied via the Tafel slope, which is determined by replottting the LSV curves as a log (j) vs. overpotential (η) [10]. The hybrid $\text{Ni}_2\text{P}-\text{MnP}@/\text{Co}_2\text{P}$ heterostructure displayed a lower Tafel slope (43.3 mV dec^{-1}) compared to the control materials, namely $\text{Ni}_2\text{P} @ \text{Co}_2\text{P}$, $\text{MnP}@/\text{Co}_2\text{P}$, and Co_2P at (77.5, 96.6, and 152.6) mV dec^{-1} , respectively. Additionally, the Tafel slope of the hybrid $\text{Ni}_2\text{P}-\text{MnP}@/\text{Co}_2\text{P}$ heterostructure (43.3 mV dec^{-1}) is quite close to the Tafel slope of Pt/C/NF (40.6 mV dec^{-1}) indicating the exceptional HER kinetics with high charge-transfer capacity of the hybrid $\text{Ni}_2\text{P}-\text{MnP}@/\text{Co}_2\text{P}$ (Fig. 3c) [26,57]. The Tafel slope of the hybrid $\text{Ni}_2\text{P}-\text{MnP}@/\text{Co}_2\text{P}$ heterostructure (43.3 mV dec^{-1}) lies in the range (40–120) mV dec^{-1} , implying the Volmer–Heyrovsky mechanism, where the Volmer step represents the rate-determining step (RDS) [57]. In the Volmer step, water dissociates into hydroxyl ion (OH^-) and adsorbed hydrogen (H^*) on the surface of the catalyst (*). In the Heyrovsky step, adsorbed hydrogen (H^*) is further associated with a water molecule to evolve molecular H_2 [19].

The Volmer–Heyrovsky step proceeds as follows:



The intrinsic activities and density of active sites determine the electrocatalytic activity of materials [26]. To the best of our knowledge, the density of electroactive sites is directly proportional to the electrochemical active surface area (ECSA) value, which insights by the electrochemical double layer capacitance (EDLC or C_{dl}) values [11]. The C_{dl} value was measured by plotting the ΔJ vs. scan rate, where, ΔJ = anodic current density (J_a) – cathodic current density (J_c) [58]. The C_{dl} value (20.21 mF cm^{-2}) of the hybrid $\text{Ni}_2\text{P}-\text{MnP}@/\text{Co}_2\text{P}$ heterostructure was calculated by conducting CV scanning with (40–100) scan rates (Fig. S13 of the SI), and further, the capacitance current versus the scan rate was plotted (Fig. 3d). The hybrid $\text{Ni}_2\text{P}-\text{MnP}@/\text{Co}_2\text{P}$ heterostructure showed the largest C_{dl} value (20.21 mF cm^{-2}), compared to the

Ni₂P @ Co₂P, MnP@Co₂P, and Co₂P of (15.45, 9.23, and 5.75) mF cm⁻², respectively. These observations implied that the superiority of HER activity is due to exposure of all active sites of the hybrid Ni₂P–MnP@Co₂P heterostructure in the electrocatalytic process, and homogeneous distribution of nanoparticles on the conductive substrate (NF) [26].

The charge-transfer resistance (R_{ct}) of the hybrid Ni₂P–MnP@Co₂P heterostructure and control materials was evaluated from Nyquist plots (Fig. 3e) of electrochemical impedance spectroscopy (EIS) [59]. The hybrid Ni₂P–MnP@Co₂P heterostructure displays much smaller semi-circular region, compared to the Ni₂P @ Co₂P, MnP@Co₂P, and Co₂P, suggesting the lower impedance (R_{ct}) of the hybrid Ni₂P–MnP@Co₂P heterostructure. As expected, the hybrid Ni₂P–MnP@Co₂P heterostructure showed a much smaller R_{ct} value (1.87 Ω), compared to those of Ni₂P @ Co₂P, MnP@Co₂P, and Co₂P of (4.47, 8.81, and 10.86) Ω , respectively, indicating superior electrical conductivity and better charge-transfer kinetics [5,11,26,43,60]. Thus, it is confirmed that the outcomes of the Tafel slope, C_{dl} , and EIS curves reveal that the integration of Ni₂P, MnP, and Co₂P in the Ni₂P–MnP@Co₂P could decrease the Tafel slope, enhance the reaction kinetics, and decrease the charge-transfer resistance of the hybrid Ni₂P–MnP@Co₂P heterostructure. As a crucial issue, the chronopotentiometry stability test was conducted for a continuous 30 h to check the practical assessment of the hybrid Ni₂P–MnP@Co₂P heterostructure. It retained 94.3% of its initial potential at a current density of 50 mA cm⁻², whereas the as-synthesized commercial Pt–C electrocatalyst retained 72.1% of its initial potential at 50 mA cm⁻², suggesting the superb stability of the Ni₂P–MnP@Co₂P.

(Fig. 3f). Similarly, the LSV plots of the hybrid Ni₂P–MnP@Co₂P heterostructure demonstrated no noticeable decrease in the overpotential after the long-term stability, before and after the 1000

continuous sweeping of the Ni₂P–MnP@Co₂P (Fig. S14 of the SI), which validates that the material is robust. The charge-transfer resistance after the long-term chronopotentiometric test was found to nearly overlap with the virgin one before stability (Fig. S15 of the SI), suggesting the consistent charge-transfer potential. Similarly, the morphology and corresponding elemental mapping of Ni₂P–MnP@Co₂P after HER stability was observed using FESEM image and FESEM-EDS, suggesting no significant change in the morphological features (Fig. S16 of the SI). The XPS analysis after HER stability showed no significant change in the XPS survey spectrum, compared to before stability (Fig. S17 of the SI). Similarly, the XPS spectra of Ni, Mn, Co, and P are almost similar to the spectra before the HER stability test, indicating the positive impact of Ni, Mn, and Co continued strong during the course of HER (Fig. S18 of the SI) [26]. The XRD pattern of Ni₂P–MnP@Co₂P was analyzed after the HER stability test (Fig. S19 of the SI). The XRD pattern after stability is almost similar to the virgin one before stability. The results obtained after the stability test confirmed the as-synthesized electrocatalyst almost retained its original electrochemical activities for HER electrocatalysis. The overall results revealed the hybrid Ni₂P–MnP@Co₂P heterostructure as a robust material towards HER, along with the long-term stability, which is superior to that of Pt–C electrocatalyst, and the recently reported phosphide-based electrocatalysts (Table S2 of the SI).

3.3.2. Oxygen evolution reaction (OER)

The OER activity of hybrid Ni₂P–MnP@Co₂P heterostructure was evaluated by linear sweep voltammograms (LSV) using the conventional three-electrode system in a 1.0 M KOH solution. For comparison, Ni₂P @ Co₂P, RuO₂, MnP@Co₂P, Co₂P, and NF were also evaluated under similar conditions. The strong redox peak around 1.35 V is attributed to the oxidation of Ni²⁺/Ni³⁺ (Fig. 4a). Ni₂P–MnP@Co₂P

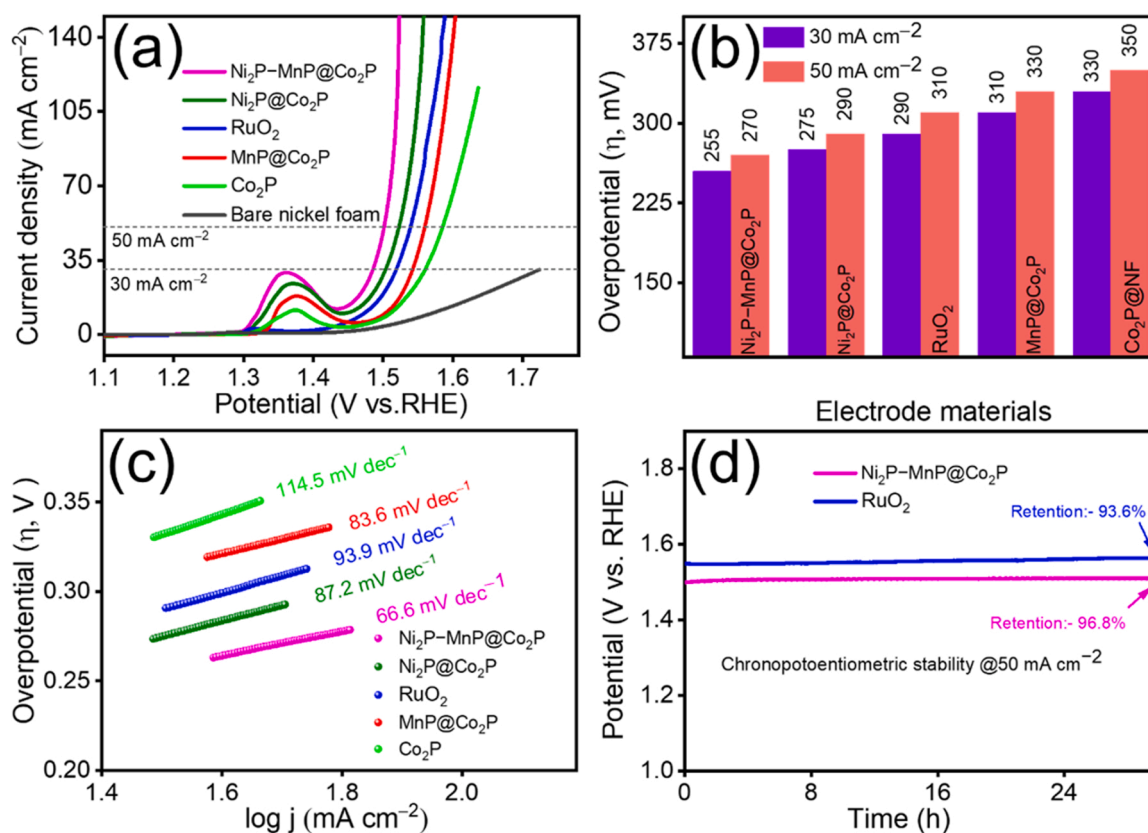


Fig. 4. Electrochemical characterization of OER activity: (a) LSV curves after iR correction of the commercial Pt/C and fabricated samples. (b) Comparative overpotential at (30 and 50) mA cm⁻² of various samples. (c) Tafel plots of different samples. (d) Chronopotentiometric curves of the Ni₂P–MnP@Co₂P and commercial RuO₂.

displayed a strong redox peak which could possibly be the better interfacial electrolyte-electrode charge transfer reaction [61]. The peak intensity gradually decreased in the order of $\text{Ni}_2\text{P} @ \text{Co}_2\text{P} > \text{MnP} @ \text{Co}_2\text{P} > \text{Co}_2\text{P}$ suggesting poorer internal conductivity compared to $\text{Ni}_2\text{P}-\text{MnP} @ \text{Co}_2\text{P}$. Hence, the LSV curve without the oxidation peak is selected to calculate OER activity [61,62]. Likewise, the reduction peaks at a potential of 1.25 V correspond to the reduction of $\text{Ni}^{3+}/\text{Ni}^{2+}$ as the LSV recorded in the negative window (Fig. S20 of the SI), and the effect on the measurement will be minimized [62–65]. As recorded in the positive scan of LSV, the reduction peak intensity decreased in the same way as observed in the positive scan. It is noticeable that the formation of equivalent redox peaks of materials on the positive and negative scans of LSV is attributed to the formation of active species during the electrochemical operation [61,63,66]. There is no change in the overpotentials of the synthesized materials @ 30 mA cm^{-2} in both the positive (Fig. 4a) and negative (Fig. S20 of the SI) scans signifying that the existence of redox oxidation peak is due to the variable valence state of transition metal elements along with the formation of ($\text{Ni}^{2+}/\text{Ni}^{3+}$, $\text{Mn}^{2+}/\text{Mn}^{3+}$, and $\text{Co}^{2+}/\text{Co}^{3+}$) couples [61,67]. The linear sweep voltammograms (LSV) polarization curve after iR correction showed that the hybrid $\text{Ni}_2\text{P}-\text{MnP} @ \text{Co}_2\text{P}$ heterostructure has the better electrocatalytic performance with overpotentials (η) = (255 and 270) mV, compared to the control materials, namely $\text{Ni}_2\text{P} @ \text{Co}_2\text{P}$ @ NF, $\text{MnP} @ \text{Co}_2\text{P}$, and Co_2P of (275 and 290, 310 and 330, and 330 and 350) mV at current densities of (30 and 50) mA cm^{-2} respectively (Fig. 4a and b). In contrast, the bare nickel foam did not exhibit noticeable OER performance. The aforementioned results strongly suggest that the interfacial interaction between the Ni_2P , MnP , and Co_2P phases was in tune with the OER electrocatalytic performance of the hybrid $\text{Ni}_2\text{P}-\text{MnP} @ \text{Co}_2\text{P}$ heterostructure, owing to the modulation of electronic structure, compared to the $\text{Ni}_2\text{P} @ \text{Co}_2\text{P}$, $\text{MnP} @ \text{Co}_2\text{P}$, and Co_2P [26,28,34,68]. In addition, the overpotential of the hybrid $\text{Ni}_2\text{P}-\text{MnP} @ \text{Co}_2\text{P}$ heterostructure is lower than those of the commercial RuO_2 catalysts of (290 and 330) mV at current densities of (30 and 50) mA cm^{-2} , respectively (Fig. 4a and b), and recently investigated OER-based electrocatalyst (Table S4 of the SI). Therefore, the improved performance of the hybrid $\text{Ni}_2\text{P}-\text{MnP} @ \text{Co}_2\text{P}$ heterostructure can be ascribed to the effective hetero-interfacial interaction of the Ni_2P , MnP , and Co_2P , as well as the synergism between $\text{Ni}_2\text{P}-\text{MnP}$ and Co_2P active sites [28,37]. Moreover, the presence of transition metal and phosphorous sites enhance the hydride acceptor and proton acceptor activity boosting the water-splitting [14,16]. Furthermore, the OER kinetic activities of the materials were estimated via the Tafel slope, which is obtained by replotting the LSV curves as a log (j) vs. overpotential (η). The hybrid $\text{Ni}_2\text{P}-\text{MnP} @ \text{Co}_2\text{P}$ heterostructure displayed a lower Tafel slope (66.6 mV dec^{-1}), compared to the control materials, namely $\text{Ni}_2\text{P} @ \text{Co}_2\text{P}$, $\text{MnP} @ \text{Co}_2\text{P}$, and Co_2P at (87.2, 83.6, and 114.5) mV dec^{-1} , respectively. Similarly, the Tafel slope of the hybrid $\text{Ni}_2\text{P}-\text{MnP} @ \text{Co}_2\text{P}$ heterostructure (66.6 mV dec^{-1}) is much less than that of the commercial RuO_2 (93.9 mV dec^{-1}), indicating the exceptional OER kinetics with the high charge-transfer capacity of $\text{Ni}_2\text{P}-\text{MnP} @ \text{Co}_2\text{P}$ (Fig. 4c). The lowest Tafel slope value of the hybrid $\text{Ni}_2\text{P}-\text{MnP} @ \text{Co}_2\text{P}$ heterostructure benefits from the hetero-interfacial interaction of different phosphides [16,30,68]. The chronopotentiometric curve of the hybrid $\text{Ni}_2\text{P} - \text{MnP} @ \text{Co}_2\text{P}$ heterostructure retained 96.8% of its initial potential at a current density of 50 mA cm^{-2} for 30 h of electrolysis, whereas the as-synthesized commercial RuO_2 @NF electrocatalyst retained 93.6% of its initial potential at 50 mA cm^{-2} , suggesting the superb stability of the $\text{Ni}_2\text{P}-\text{MnP} @ \text{Co}_2\text{P}$ (Fig. 4d). Similarly, the LSV of the hybrid $\text{Ni}_2\text{P}-\text{MnP} @ \text{Co}_2\text{P}$ heterostructure demonstrated no noticeable variation in the overpotential after 1000 continuous sweeping cycles, and after the long-term chronopotentiometry analysis, strongly suggesting the superior stability of the material (Fig. S21 of the SI). The Nyquist plots presented in Fig. S22 of the SI reveal no significant changes in the charge-transfer resistance of $\text{Ni}_2\text{P}-\text{MnP} @ \text{Co}_2\text{P}$ after OER stability. Similarly, the morphology and the

respective elemental mapping of $\text{Ni}_2\text{P}-\text{MnP} @ \text{Co}_2\text{P}$ after OER stability was inspected using FESEM image and FESEM-EDS, proving no significant change in the morphological features (Fig. S23 of the SI), except some increased roughness, possibly due to the mild corrosion with strong base. The XPS analysis after OER stability showed no significant changes in the XPS survey spectrum, compared to before stability (Fig. S24a of the SI). The XPS spectra of Co (Fig. S24d of the SI) is almost similar to the spectra before the OER stability test of the original one. However, the slight change in the XPS spectrum of Ni 2p and Mn 3d was inspected after the OER stability test (Fig. S24b and c of the SI). The Ni^{6+} peak is almost invisible, and the additional peak at 858.2 eV is ascribed to the in situ formation of NiOOH . The peak at 874.6 eV corresponds to the satellite peak (Fig. S24b of the SI) [69]. The XPS spectra of Mn obviously shifted to higher binding energy of (641.6 and 652.9, 643.3 and 652.9, and 646.3 and 655.7) eV for Mn^{2+} , Mn^{3+} , and Mn^{4+} , respectively, due to surface reorganization during the electrochemical OER process (Fig. S24c of the SI) [18,23,26]. The XPS spectrum P 2p showed the reduction of P 2p_{3/2}, and P 2p_{1/2} spectrum, while that of P–O is increased, suggesting that the superficial oxidation of electrocatalyst in the alkaline medium is in agreement with the experimental results (Fig. S24e of the SI) [14,22,26]. The XPS spectra of O 1 s displayed the three peaks at binding energies of (530.88, 531.78, and 533.48) eV, which suggest the formation of M–O, O–O, and O–OH bonds, respectively (Fig. S24f of the SI) [26]. Interestingly, the NiOOH of the electrocatalyst could be the active sites along with Ni_2P , MnP , and Co_2P , to further enhance the OER electrocatalytic activities [22,23]. The XRD pattern after stability test (Fig. S19 of the SI) is almost similar to the virgin one before stability. However, some additional peaks of nickel oxyhydroxide (NiOOH) at (28.1 and 35.57) $^\circ$ (Reference code: 00–027–0956) were detected, due to the formation of oxy hydroxides of nickel on the surface of the electrode during the chronopotentiometric test [70].

Moreover, no noticeable peaks of manganese oxyhydroxide (MnOOH) were observed, indicating no obvious oxidation of manganese [23,25,26]. The surface reorganization during the electrochemical OER process was further convinced with in situ Raman spectrochemical analysis. During the initial CV cycle, the nature of in situ Raman spectra showed different patterns with an increase in the applied potential from 0.98 V to 1.58 V vs. RHE. When CV operated upon positive scan, the observed spectra showed two different peaks of NiOOH at 482 cm^{-1} (E_g - bending vibration) and 558 cm^{-1} (A_1g - stretching vibration) regions at potential 1.38 V vs. RHE and the intensity of NiOOH peaks enhanced at potentials 1.48 and 1.58 V vs. RHE gradually (Fig. S26a of the SI) [65, 71]. Likewise, when CV operated upon negative scan, the peak intensity decreased with decrease in the applied potential from 1.58 to 1.38 V vs. RHE. After 1.38 V, the similar patterns were observed as recorded on positive scan which is in agreement with reported electrocatalyst (Fig. S26b of the SI) [65]. Furthermore, the in situ Raman spectra were observed during the 50th CV cycle, the more intense peaks were observed than that of recorded during first CV cycle (Fig. S26c of the SI). When CV was operated in negative scan, the intense peaks were reversed in order than that of observed in positive scan rate (Fig. S26d of the SI). Overall, in situ Raman spectra of as-synthesized electrodes demonstrated typical Raman peaks of NiOOH at 482 cm^{-1} (E_g) and 558 cm^{-1} (A_1g) (Fig. S25 of the SI), indicating that NiOOH is a possible active phase in electrochemical OER activity, which is in agreement with the previous literature [65,71–73]. Furthermore, the in situ Raman spectra of $\text{Ni}_2\text{P}-\text{MnP} @ \text{Co}_2\text{P}$ after 1000th CV cycle (Fig. S26e and f of the SI) demonstrated no significant fluctuation compared to that obtained during the 50th CV cycle, which confirmed that the restructured NiOOH still continues in the OER activities [65]. Additionally, the results are further corroborated by the TEM and XPS analysis. The results reveal the good retention of the material regarding the physicochemical properties after long-term durability operation towards OER. Hence, the hybrid $\text{Ni}_2\text{P}-\text{MnP} @ \text{Co}_2\text{P}$ heterostructure as robust electrode material demonstrated the excellent OER performances of the phosphide-based

electrocatalysts (Table S4 of the SI).

3.3.3. DFT analysis for HER and OER mechanism

To understand the mechanism for electrochemical performance enhancement of $\text{Ni}_2\text{P}-\text{MnP}@/\text{Co}_2\text{P}$ compared to other counterparts, we performed the calculation of projected density of states (PDOS) and Gibbs free energy with the different models (Fig. 5a-c).

Interestingly, a high value of electronic DOS at the Fermi energy level and free energy absorption of hydrogen (ΔG_{H}^*) value near 0.0 eV are believed as essential objectives to demonstrate excellent catalytic activity. Hence, ΔG_{H}^* and DOS of the aforementioned models were analyzed using the DFT system [27]. The $\text{Ni}_2\text{P}-\text{MnP}@/\text{Co}_2\text{P}$ holds a high DOS at the Fermi level in compared to $\text{Ni}_2\text{P}@/\text{Co}_2\text{P}$ and $\text{MnP}@/\text{Co}_2\text{P}$, suggesting the higher electron transport ability and accelerate the charge-transfer kinetics [74]. In addition, the adsorption ability of H^* and intermediated O species on the catalysts surface was investigated. The absolute $|\Delta G_{\text{H}}|$ of $\text{Ni}_2\text{P}-\text{MnP}@/\text{Co}_2\text{P}$ exhibited the smallest value of 0.09 eV, which is superior to other constructed models of $\text{Ni}_2\text{P}@/\text{Co}_2\text{P}$ (0.17 eV) and $\text{MnP}@/\text{Co}_2\text{P}$ (0.35 eV), illustrating the

enhancement of HER (Fig. 6a) [75,76]. In order to examine the OER performance, we composed the adsorption of oxygen species on the catalysts surface model [27]. Theoretical overpotential was revealed from the rate-determining step (RDS) during the OER process [77]. As shown in Fig. 6b, RDS of $\text{Ni}_2\text{P}-\text{MnP}@/\text{Co}_2\text{P}$ catalyst showed a small RDS of 1.86 V, which was associated with the transformation of O^* into HOO^* step [27,77]. The corresponding overpotential was estimated of 0.63 V at the active Co sites of Co_2P shell, which is better than $\text{Ni}_2\text{P}@/\text{Co}_2\text{P}$ (0.90 V) and $\text{MnP}@/\text{Co}_2\text{P}$ (1.19 V), respectively. This result further confirmed the synergistic effect of heterogeneous $\text{Ni}_2\text{P}-\text{MnP}$ at the core nanostructure could significantly decrease the Gibbs free energy barrier and therefore it could accelerate the adsorption of oxygen species and boost the oxygen evolution process.

3.3.4. Overall water-splitting

Based on the observed excellent HER and OER performances of the hybrid $\text{Ni}_2\text{P}-\text{MnP}@/\text{Co}_2\text{P}$ heterostructure, the eligibility of the hybrid $\text{Ni}_2\text{P}-\text{MnP}@/\text{Co}_2\text{P}$ heterostructure was further inspected as a bifunctional material for use as both the anode and cathode for water-splitting

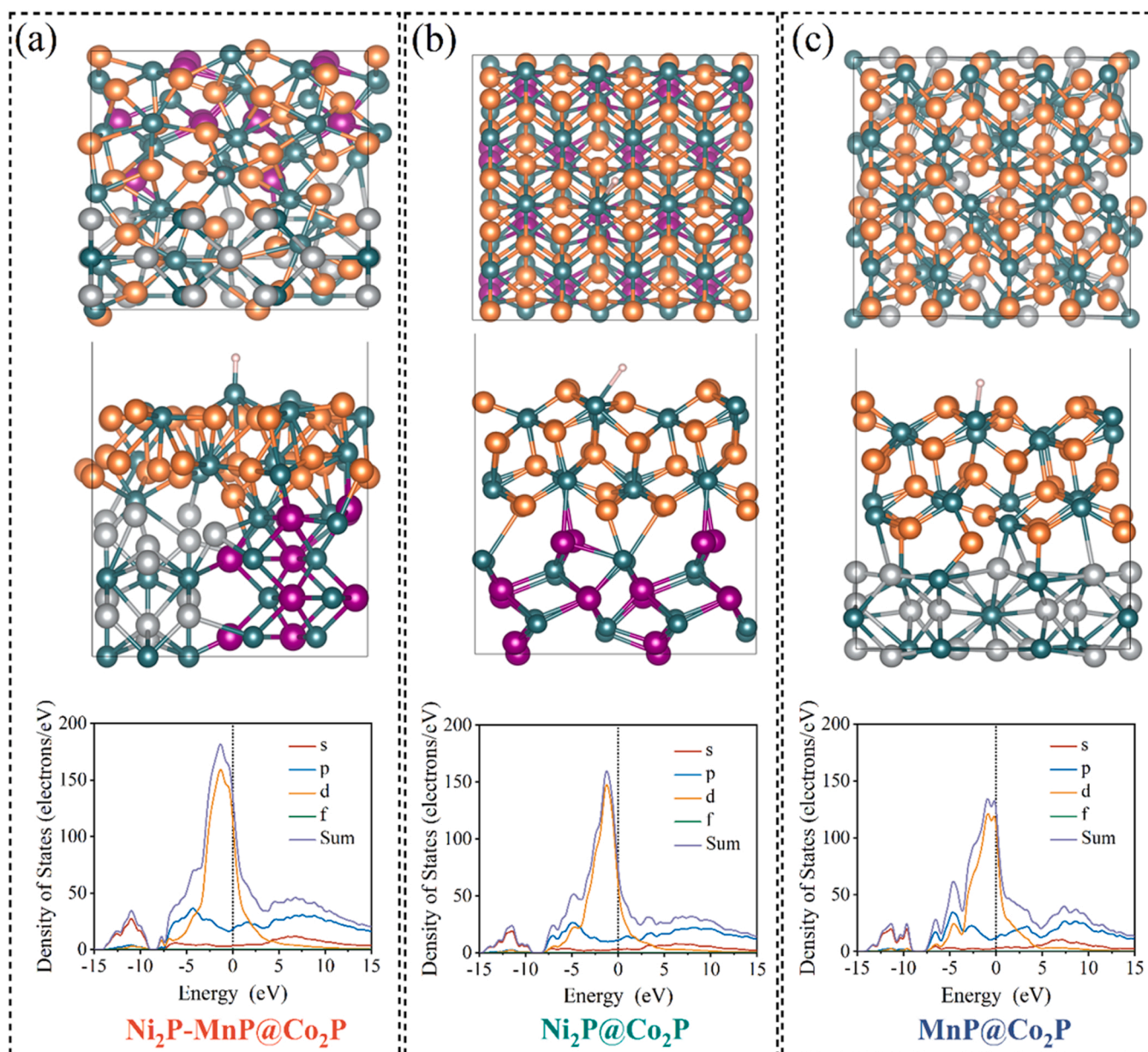


Fig. 5. The modeling and the corresponding calculated PDOS of (a) $\text{Ni}_2\text{P}-\text{MnP}@/\text{Co}_2\text{P}$, (b) $\text{Ni}_2\text{P}@/\text{Co}_2\text{P}$, and (c) $\text{MnP}@/\text{Co}_2\text{P}$.

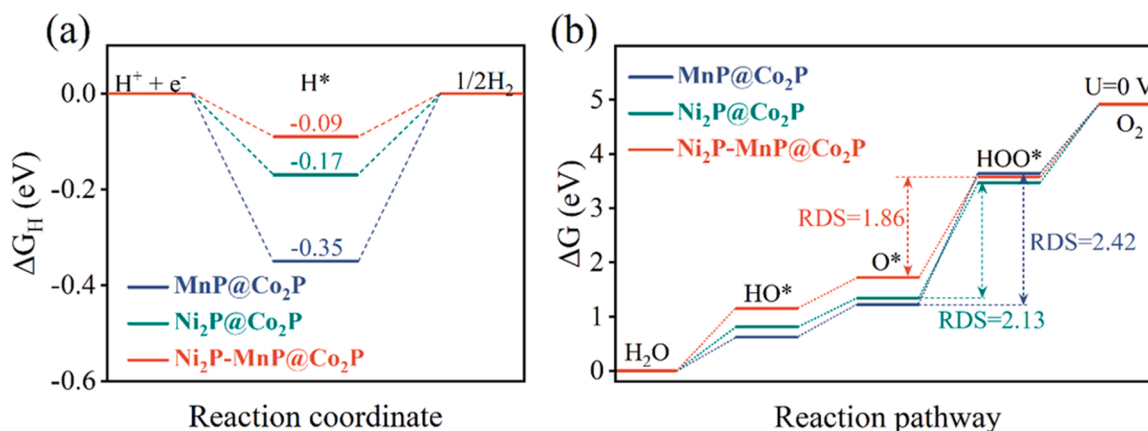


Fig. 6. The Gibb free energy diagram at different stage of H₂O dissociation for the hydrogen and oxygen evolution of (a) Ni₂P–MnP@Co₂P, (b) Ni₂P @ Co₂P, and (c) MnP@Co₂P.

in alkaline electrolyte. The evolution of hydrogen and oxygen gases is shown in a digital image of the device (Fig. 7a). Fig. 7b showed the polarization curves of the Ni₂P–MnP@Co₂P (+,–) device and the reference RuO₂//Pt–C for the overall water-splitting. The LSV curve of the Ni₂P–MnP@Co₂P (+,–) electrolyzer before the stability test showed lower cell voltage (1.50 V), compared to the commercial RuO₂//Pt–C (1.54 V), depicting the better electrochemical activities of the Ni₂P–MnP@Co₂P. As reported electrocatalysts, the overall water splitting performed by the electrolyzer exhibited different cell potentials due to some operating conditions and the choice of the electrode materials.

Particularly, it depends on the precursor amount, temperature and concentration of the electrolytic medium [50,51]. Moreover, the precursor purity, mass loading, and electrode designing method affect the overall water splitting performance [52]. In the same way, Ni₂P–MnP@Co₂P showed the anticipated similarity of cell voltage (1.50 V @ 10 mA cm^{–2}) to the reported literatures [61,77–82] (Table S5 of the SI). The chronoamperometric stability curve of the alkaline Ni₂P–MnP@Co₂P (+,–) electrolyzer retained 96.8% of its initial current density at 10 mA cm^{–2} for 50 h, whereas the commercial RuO₂//Pt–C retained 73.2% of its initial current density, suggesting the

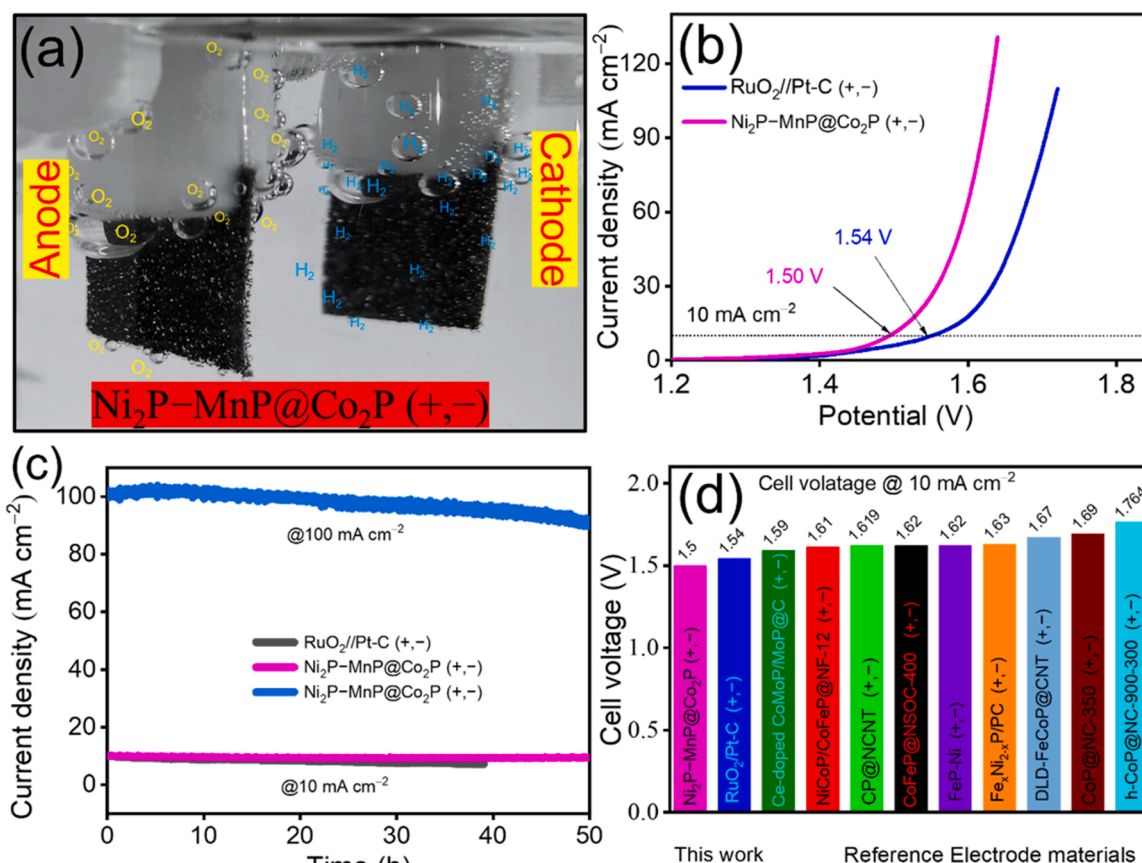


Fig. 7. Performance of the overall water-splitting device: (a) Digital photograph of the designed Ni₂P–MnP@Co₂P (+,–) alkaline electrolyzer. (b) LSV curves of Ni₂P–MnP@Co₂P (+,–) and commercial RuO₂//Pt–C (+,–) before Chronoamperometric test. (c) Chronoamperometric curves of the Ni₂P–MnP@Co₂P (+,–) and RuO₂//Pt–C (+,–). (d) Comparison of cell voltage at 10 mA cm^{–2} for the Ni₂P–MnP@Co₂P (+,–) and RuO₂//Pt–C (+,–) with various reported electrolyzers.

superior durability of $\text{Ni}_2\text{P}-\text{MnP}@-\text{Co}_2\text{P}$ (+,-). Likewise, to further validate the robust stability of the $\text{Ni}_2\text{P}-\text{MnP}@-\text{Co}_2\text{P}$ (+,-), chronoamperometry stability test at 100 mA cm^{-2} was performed. The result still showed outstanding durability despite a negligible drop in retention (91.12%) compared to the at 10 mA cm^{-2} , which proves the astonishing stability of the material (Fig. 7c). Furthermore, the LSV curve after the chronoamperometry test displayed no further significant change in the initial cell voltage, indicating the superb bifunctional potential of the $\text{Ni}_2\text{P}-\text{MnP}@-\text{Co}_2\text{P}$ electrode (Fig. S27 of the SI [26,30,32]). From the results, it is concluded that the $\text{Ni}_2\text{P}-\text{MnP}@-\text{Co}_2\text{P}$ (+,-) device can perform superb bifunctional electrocatalytic activities toward both the HER and OER, compared to the recently reported electrocatalysts (Table S6 of the SI). The superior electrocatalytic activities towards the overall water-splitting is the result of the presence of multi-active sites (nickel phosphide, manganese phosphide, and cobalt phosphide) [14]. More imposing is the fact that the performance of the hybrid $\text{Ni}_2\text{P}-\text{MnP}@-\text{Co}_2\text{P}$ heterostructure electrode surpasses that of the as-fabricated commercial alkaline electrolyzer $\text{RuO}_2//\text{Pt}-\text{C}$ device [19, 26]. Inspired by the outstanding performance of $\text{Ni}_2\text{P}-\text{MnP}@-\text{Co}_2\text{P}$ (+,-), we further designed a single stack cell electrolyzer (cathode and anode) of fabricated $\text{Ni}_2\text{P}-\text{MnP}@-\text{Co}_2\text{P}$. The electrolyzer consists of gas diffusion layers (bare NF), an electrode (anode and cathode), membrane, current collector (stainless plate) as displayed in the Fig. 8a. As shown in Fig. 8a, one peristaltic pump was connected to supply electrolytic solution from reservoirs into anode. The LSV curve in Fig. 8b displayed the cell potential 1.69 V to attain 100 mA cm^{-2} (1.0 M KOH, at room temperature) which is slightly higher than the cell potential observed in the two electrode membrane free electrolyzer ($1.62 @ 100 \text{ mA cm}^{-2}$). The reason behind the increase in potential

using single stack cell electrolyzer is attributed to resistance caused by membrane which is in agreement to reported electrodes [64,83,84]. Furthermore, the long-term CP stability test of $\text{Ni}_2\text{P}-\text{MnP}@-\text{Co}_2\text{P}$ (+,-) was conducted for 50 h at 100 mA cm^{-2} (1.0 M KOH) which demonstrated that the no significant change in the cell potential as displayed in Fig. 8c. The robustness of electrode material was further confirmed by measuring LSV potential after CP test and was found to be no significant change than that of potential before stability (Fig. 8d). Based on the results, we can conclude that the as-synthesized hybrid $\text{Ni}_2\text{P}-\text{MnP}@-\text{Co}_2\text{P}$ heterostructure electrocatalyst has great potential and can be used practically for overall water splitting. The quantity of evolved (H_2/O_2) gas can be calculated by integration from the chronopotentiometry analysis, from which the Faradaic efficiency was determined using a $\text{Ni}_2\text{P}-\text{MnP}@-\text{Co}_2\text{P}$ (+,-) lab-made device. Here, the hybrid $\text{Ni}_2\text{P}-\text{MnP}@-\text{Co}_2\text{P}$ heterostructure was used as both the anode and cathode (Fig. S28 of the SI). The chronopotentiometry was performed at 50 mA cm^{-2} for 6 h. The obtained volume of H_2/O_2 gas was noted by monitoring the volume of displaced water and calculating the quantity of evolved H_2/O_2 gas. The Faradaic efficiency was determined as (97.2 and 97.9) % at 50 mA cm^{-2} for H_2 and O_2 , respectively. Meanwhile, the morphological features of the hybrid $\text{Ni}_2\text{P}-\text{MnP}@-\text{Co}_2\text{P}$ heterostructure after the long-term stability test were examined by FESEM, and TEM, analysis. FESEM in Fig. S29 of the SI displayed no significant variation in the morphology of the cathodic $\text{Ni}_2\text{P}-\text{MnP}@-\text{Co}_2\text{P}$ electrode. Similarly, the TEM image and the respective element mapping (Fig. S30 of the SI) also demonstrated no substantial changes in the cathodic $\text{Ni}_2\text{P}-\text{MnP}@-\text{Co}_2\text{P}$ electrode compared to the original one before overall water splitting. Furthermore, FESEM imagery of anodic $\text{Ni}_2\text{P}-\text{MnP}@-\text{Co}_2\text{P}$ electrode showed no significant changes, except some negligibly

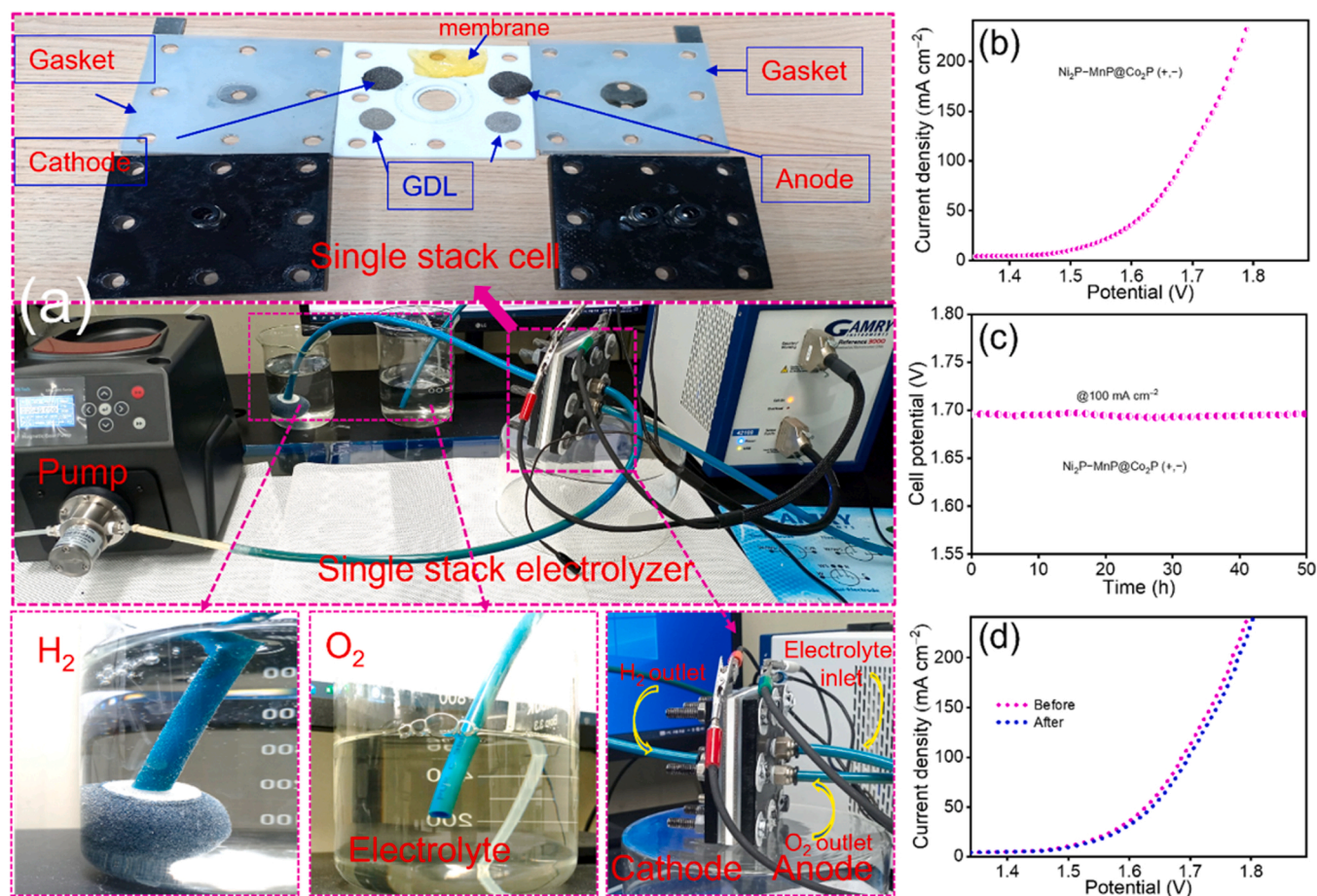


Fig. 8. (a) Digital photograph of the experimental system of single stack electrolyzer ($\text{Ni}_2\text{P}-\text{MnP}@-\text{Co}_2\text{P}$ (+,-)). (b) LSV curve displaying the cell potential $\text{Ni}_2\text{P}-\text{MnP}@-\text{Co}_2\text{P}$ (+,-) toward overall water splitting. (c) long-term stability test at constant 100 mA cm^{-2} . (d) LSV curves before and after stability test.

observed rough surfaces (Fig. S31 of the SI). Nevertheless, the TEM, HRTEM, STEM, and elemental distribution imagery (Fig. S32 of the SI) showed the absolute similarity with the original one, which could be due to the mutually arranged heterostructure of Ni_2P – MnP and Co_2P having close contact between substrate and electrocatalyst [26]. To confirm the surface reconstruction of anodic (OER) electrode after long-term durability test, the HRTEM study was further analyzed as presented in Fig. S32 of the SI. Compared to the virgin one, an insignificant change in the HRTEM image of the anodic electrode was observed. In the HRTEM image, along with Ni_2P , MnP , and Co_2P lattice phases, lattice fringe with an interplanar distance of 0.239 nm corresponding to a plane (011) of NiOOH was detected which is analogous to the additional peak observed at $2\theta = 35.57^\circ$ in the XRD analysis (Fig. S25 of the SI) of post OER electrode, as earlier reported literature. The formation of oxyhydroxides of Ni on the surface of the Ni_2P – MnP @ Co_2P electrode during the electrochemical test further enhances the OER electrochemical activities as reported earlier electrocatalysts [19,23,80,85].

In addition, surface reconstruction on cathodic electrode was studied using XPS analysis which displayed no substantial fluctuation of Ni 2p, Mn 2p, Co 2p, and P 2p spectrums compared to the virgin electrodes XPS spectrums (Fig. S33 of the SI).

It is also notified that the binding energies of Ni 2p, Mn 2p, Co 2p, and P 2p of cathodic electrode used in OWS are almost similar to the XPS spectrums of the virgin electrode (and even similar to the XPS spectra of HER electrode (after CP test) in Fig. S18 of the SI suggesting the no changed in the surface structure of cathodic electrode. In addition, surface reconstruction on anodic electrode was studied using XPS analysis of Ni 2p, Mn 2p, Co 2p, and P 2p spectrum (Fig. S33 of the SI). The XPS spectra of Co 2p (Fig. S33c of the SI) displayed almost similar BE as observed in virgin electrode. Though the slight variation in the XPS spectrums of (Ni 2p and Mn 2p) was scrutinized after the OWS stability test (Fig. S33a and b of the SI). The Ni^{2+} peak is almost undetectable, and the additional peak at 858.32 eV is attributed to the in situ formation of NiOOH . The peak at 874.66 eV corresponds to the satellite peak (Fig. S33a of the SI) [69]. Interestingly, the developed oxyhydroxide (-OOH) of nickel on the electrode could be the active sites along with Ni_2P , MnP , and Co_2P , to further enhance the anodic electrode activities for OER during OWS operation [22,23]. The XPS spectra of Mn obviously shifted to higher binding energy of (641.66 and 653.13, 643.32 and 654.57, and 646.46 and 655.76) eV for Mn^{2+} , Mn^{3+} , and Mn^{4+} , respectively, due to surface reorganization during the electrochemical OWS process (Fig. S33b of the SI) [18,23,26]. The XPS P 2p spectrum displayed the drop of P 2p_{3/2} and P 2p_{1/2} spectrums intensities, while that of P–O is heightened, suggesting that the superficial oxidation of electrode in the alkaline medium (Fig. S33d of the SI) [14, 22,26]. Overall, the hybrid Ni_2P – MnP @ Co_2P heterostructure showed good preservation of the morphology, proving it as a robust electrode material for overall water-splitting.

In brief analysis, the hybrid Ni_2P – MnP @ Co_2P heterostructure electrocatalyst is a decent contender for electrochemical water-splitting, and its respectable electrocatalytic activities can be ascribed to the following reasons: (1) The formation of a unique heterostructure significantly enhances the specific surface area of the catalyst, further offering plentiful exposed electrocatalytic active sites.

(2) The intense coupling heterointerfaces between the Ni_2P – MnP nanosheet and Co_2P nanoflower provide electron and mass transfer, efficiently creating synergy among the real active sites of Ni_2P – MnP , Ni_2P , MnP , and Co_2P with the regulation of electronic structure, which boosts the equilibrium adsorption of hydrogen (H^*) and oxygen ($^*\text{OH}$) intermediates. (3) The integration of multi-metals Ni, Mn, and Co enhances the reconstruction of the electronic structure of the electrocatalyst, which could be effective to increase the electrochemical properties. (4) The minimal charge-transfer, as well as electrolytic resistance of the unique architecture imply the effective charge transport capacity of the Ni_2P – MnP @ Co_2P via the integration of Ni_2P – MnP nanosheets and Co_2P nanoflower. (5) The facile strategy efficiently

avoids the use of binders, which both improves the reaction kinetics, and provides good mechanical adhesion to boost the electrocatalytic activity. These characteristics are expected to be suitable reasons underlying the outstanding HER, OER, and overall water-splitting performance of the hybrid Ni_2P – MnP @ Co_2P heterostructure.

4. Conclusions

In summary, the hybrid Ni_2P – MnP @ Co_2P heterostructure electrocatalyst is effectively synthesized using a facile hydrothermal route, followed by the control CVD process. The superior performance of the hybrid Ni_2P – MnP @ Co_2P heterostructure can rival the state-of-art catalysts, achieving $\eta = (60 \text{ and } 255) \text{ mV}$ for HER (10 mA cm^{-2}) and OER (30 mA cm^{-2}) with Tafel slopes of (43.3 and 66.6) mV dec^{-1} , respectively. The hybrid Ni_2P – MnP @ Co_2P heterostructure can be employed for both anodic and cathodic electrodes with a low cell voltage of 1.50 V at 10 mA cm^{-2} , emphasizing the superior efficiency of the catalyst. The outstanding long-term stability of the Ni_2P – MnP @ Co_2P (+,–) alkaline electrolyzer for 50 h operation indicates great potential for large-scale green H_2 and O_2 production. Hence, this work manifests a novel perspective for designing the efficient bifunctional electrocatalysts to replace highly expensive noble metal-based electrolyzers.

CRediT authorship contribution statement

Mani Ram Kandel: Conceptualization, Methodology, Investigation, Formal analysis, Validation, Writing – original draft. **Uday Narayan Pan:** Methodology, Data curation, Formal analysis, Visualization, Conceptualization, Writing - review & editing. **Purna Prasad Dhakal:** Methodology, Data curation, Visualization. **Ram Babu Ghising:** Methodology, Data curation, Visualization. **Junhuan Zhao:** Data curation, Visualization. **Nam Hoon Kim:** Conceptualization, Data curation, Writing – review & editing, Supervision. **Joong Hee Lee:** Conceptualization, Writing – review & editing, Supervision, Project administration.

Declaration of Competing Interest

The authors declare that they have no known competing financial interests or personal relationships that could have appeared to influence the work reported in this paper.

Data Availability

Data will be made available on request.

Acknowledgements

This work was supported by the Basic Science Research Program (2022R1A2C2010339) and the Regional Leading Research Center Program (2019R1A5A8080326) through the National Research Foundation funded by the Ministry of Science and ICT of the Republic of Korea.

Appendix A. Supporting information

Supplementary data associated with this article can be found in the online version at doi:10.1016/j.apcatb.2023.122680.

References

- [1] J. Chow, R.J. Kopp, P.R. Portney, Energy resources and global development, *Science* 80 (302) (2003) 1528–1531, <https://doi.org/10.1126/science.1091939>.
- [2] S. Chu, A. Majumdar, Opportunities and challenges for a sustainable energy future, *Nature* 488 (2012) 294–303, <https://doi.org/10.1038/nature11475>.
- [3] M.S. Dresselhaus, I. Thomas, Dresselhaus, *Nature* 414 (2001) 332–337 (www.nature.com).
- [4] S. Chu, Y. Cui, N. Liu, The path towards sustainable energy, *Nat. Mater.* 16 (2016) 16–22, <https://doi.org/10.1038/nmat4834>.

- [5] J. Zhu, L. Hu, P. Zhao, L.Y.S. Lee, K.Y. Wong, Recent advances in electrocatalytic hydrogen evolution using nanoparticles, *Chem. Rev.* 120 (2020) 851–918, <https://doi.org/10.1021/acs.chemrev.9b00248>.
- [6] S. Anantharaj, S.R. Ede, K. Sakthikumar, K. Karthick, S. Mishra, S. Kundu, Recent trends and perspectives in electrochemical water splitting with an emphasis on sulfide, selenide, and phosphide catalysts of Fe, Co, and Ni: a review, *ACS Catal.* 6 (2016) 8069–8097, <https://doi.org/10.1021/acscatal.6b02479>.
- [7] Y. Pei, Y. Cheng, J. Chen, W. Smith, P. Dong, P.M. Ajayan, M. Ye, J. Shen, Recent developments of transition metal phosphides as catalysts in the energy conversion field, *J. Mater. Chem. A* 6 (2018) 23220–23243, <https://doi.org/10.1039/C8TA09454C>.
- [8] H.T. Le, D.T. Tran, T.H. Nguyen, V.A. Dinh, N.H. Kim, J.H. Lee, Single platinum atoms implanted 2D lateral anion-intercalated metal hydroxides of $\text{Ni}_2(\text{OH})_2(\text{NO}_3)_2$ as efficient catalyst for high-yield water splitting, *Appl. Catal. B Environ.* 317 (2022), 121684, <https://doi.org/10.1016/j.apcatb.2022.121684>.
- [9] J. Wang, D.T. Tran, K. Chang, S. Prabhakaran, D.H. Kim, N.H. Kim, J.H. Lee, Atomic heterointerface engineering of nickel selenide confined nickel molybdenum nitride for high-performance solar-driven water splitting, *Energy Environ. Mater.* (2022) 0–3, <https://doi.org/10.1002/eem2.12526>.
- [10] C.C. Gudal, U.N. Pan, D.R. Paudel, M.R. Kandel, N.H. Kim, J.H. Lee, Bifunctional P-intercalated and doped metallic (1T)-copper molybdenum sulfide ultrathin 2D-nanosheets with enlarged interlayers for efficient overall water splitting, *ACS Appl. Mater. Interfaces* 14 (2022) 14492–14503, <https://doi.org/10.1021/acsaami.2c00278>.
- [11] M.R. Kandel, U.N. Pan, D.R. Paudel, P.P. Dhakal, N.H. Kim, J.H. Lee, Hybridized bimetallic phosphides of Ni–Mo, Co–Mo, and Co–Ni in a single ultrathin-3D-nanosheets for efficient HER and OER in alkaline media, *Compos. Part B Eng.* 239 (2022), 109992, <https://doi.org/10.1016/j.compositesb.2022.109992>.
- [12] R.B. Ghising, U.N. Pan, D.R. Paudel, M.R. Kandel, N.H. Kim, J.H. Lee, A hybrid trimetallic-organic framework-derived N, C co-doped Ni–Fe–Mn–P ultrathin nanosheet electrocatalyst for proficient overall water-splitting, *J. Mater. Chem. A* 10 (2022) 16457–16467, <https://doi.org/10.1039/D2TA02470E>.
- [13] Z. Pu, T. Liu, L.S. Amini, R. Cheng, P. Wang, C. Zhang, P. Ji, W. Hu, J. Liu, S. Mu, Transition-metal phosphides: activity origin, energy-related electrocatalysis applications, and synthetic strategies, *Adv. Funct. Mater.* 30 (2020) 1–23, <https://doi.org/10.1002/adfm.202004009>.
- [14] E. Vijayakumar, S. Ramakrishnan, C. Sathikumar, D.J. Yoo, J. Balamurugan, H. S. Noh, D. Kwon, Y.H. Kim, H. Lee, MOF-derived CoP-nitrogen-doped carbon@NiFeP nanoflakes as an efficient and durable electrocatalyst with multiple catalytically active sites for OER, HER, ORR and rechargeable zinc-air batteries, *Chem. Eng. J.* 428 (2022), 131115, <https://doi.org/10.1016/j.cej.2021.131115>.
- [15] Y. Guo, J. Tang, Z. Wang, Y. Sugahara, Y. Yamauchi, Hollow porous heterometallic phosphide nanocubes for enhanced electrochemical water splitting, *Small* 14 (2018) 1–8, <https://doi.org/10.1002/smll.201802442>.
- [16] J. Lin, Y. Yan, C. Li, X. Si, H. Wang, J. Qi, J. Cao, Z. Zhong, W. Fei, J. Feng, Bifunctional electrocatalysts based on Mo-doped NiCoP nanosheet arrays for overall water splitting, *Nano-Micro Lett.* 11 (2019) 1–11, <https://doi.org/10.1007/s40820-019-0289-6>.
- [17] N. Jiang, B. You, M. Sheng, Y. Sun, Electrodeposited cobalt-phosphorous-derived films as competent bifunctional catalysts for overall water splitting, *Angew. Chem. - Int. Ed.* 54 (2015) 6251–6254, <https://doi.org/10.1002/anie.201501616>.
- [18] H. Xiang, W. Chen, T. Li, J. Huang, G. Chen, T. Gong, K. Ken Ostrikov, High-performance CoNb phosphide water splitting electrocatalyst on plasma-defect-engineered carbon cloth, *Chem. Eng. J.* 446 (2022), 137419, <https://doi.org/10.1016/j.cej.2022.137419>.
- [19] M.A.R. Anjum, M.S. Okyay, M. Kim, M.H. Lee, N. Park, J.S. Lee, Bifunctional sulfur-doped cobalt phosphide electrocatalyst outperforms all-noble-metal electrocatalysts in alkaline electrolyzer for overall water splitting, *Nano Energy* 53 (2018) 286–295, <https://doi.org/10.1016/j.nanoen.2018.08.064>.
- [20] M.A.R. Anjum, J.S. Lee, Sulfur and nitrogen dual-doped molybdenum phosphide nanocrystallites as an active and stable hydrogen evolution reaction electrocatalyst in acidic and alkaline media, *ACS Catal.* 7 (2017) 3030–3038, <https://doi.org/10.1021/acscatal.7b00555>.
- [21] D. Chen, Z. Xu, W. Chen, G. Chen, J. Huang, C. Song, K. Zheng, Z. Zhang, X. Hu, H. S. Choi, K. Ostrikov, Mulberry-inspired nickel-niobium phosphide on plasma-defect-engineered carbon support for high-performance hydrogen evolution, *Small* 16 (2020) 1–9, <https://doi.org/10.1002/smll.202004843>.
- [22] M. Baek, G.W. Kim, T. Park, K. Yong, NiMoFe and NiMoFeP as complementary electrocatalysts for efficient overall water splitting and their application in PV-electrolysis with STH 12.3%, *Small* 15 (2019) 1–11, <https://doi.org/10.1002/smll.201905501>.
- [23] M. Liu, Z. Sun, S. Li, X. Nie, Y. Liu, E. Wang, Z. Zhao, Hierarchical superhydrophilic/superaerophobic CoMnP/Ni₂P nanosheet-based microplate arrays for enhanced overall water splitting, *J. Mater. Chem. A* 9 (2021) 22129–22139, <https://doi.org/10.1039/d1ta04713b>.
- [24] C.G. Read, J.F. Callejas, C.F. Holder, R.E. Schaak, General strategy for the synthesis of transition metal phosphide films for electrocatalytic hydrogen and oxygen evolution, *ACS Appl. Mater. Interfaces* 8 (2016) 12798–12803, <https://doi.org/10.1021/acsaami.6b02352>.
- [25] L. Ji, Y. Wei, P. Wu, M. Xu, T. Wang, S. Wang, Q. Liang, T.J. Meyer, Z. Chen, Heterointerface Engineering of Ni₂P-Co₂P nanoframes for efficient water splitting, *Chem. Mater.* 33 (2021) 9165–9173, <https://doi.org/10.1021/acs.chemmater.1c02609>.
- [26] S. Singh, D.C. Nguyen, N.H. Kim, J.H. Lee, Interface engineering induced electrocatalytic behavior in core-shelled CNT_s@Ni₂P/NbP heterostructure for highly efficient overall water splitting, *Chem. Eng. J.* 442 (2022), 136120, <https://doi.org/10.1016/j.cej.2022.136120>.
- [27] K. Chang, D.T. Tran, J. Wang, S. Prabhakaran, D.H. Kim, N.H. Kim, J.H. Lee, Atomic heterointerface engineering of Ni₂P-NiSe₂ nanosheets coupled ZnP-based arrays for high-efficiency solar-assisted water splitting, *Adv. Funct. Mater.* 32 (2022), 2113224, <https://doi.org/10.1002/adfm.202113224>.
- [28] D. Zheng, L. Yu, W. Liu, X. Dai, X. Niu, W. Fu, W. Shi, F. Wu, X. Cao, Structural advantages and enhancement strategies of heterostructure water-splitting electrocatalysts, *Cell Rep. Phys. Sci.* 2 (2021), 100443, <https://doi.org/10.1016/j.xcrp.2021.100443>.
- [29] D.C. Nguyen, D.T. Tran, T.L.L. Doan, D.H. Kim, N.H. Kim, J.H. Lee, Rational design of Core@shell structured CoS_x@Cu₂MoS₄ hybridized MoS₂/N,S-codoped graphene as advanced electrocatalyst for water splitting and Zn-Air battery, *Adv. Energy Mater.* 10 (2020), 1903289, <https://doi.org/10.1002/aenm.201903289>.
- [30] C. Du, M. Shang, J. Mao, W. Song, Hierarchical MoP/Ni₂P heterostructures on nickel foam for efficient water splitting, *J. Mater. Chem. A* 5 (2017) 15940–15949, <https://doi.org/10.1039/c7ta03669h>.
- [31] S. Wen, G. Chen, W. Chen, M. Li, B. Ouyang, X. Wang, D. Chen, T. Gong, X. Zhang, J. Huang, K. (Ken) Ostrikov, Nb-doped layered FeNi phosphide nanosheets for highly efficient overall water splitting under high current densities, *J. Mater. Chem. A* 9 (2021) 9918–9926, <https://doi.org/10.1039/d1ta00372k>.
- [32] X. Bu, R. Wei, W. Gao, C. Lan, J.C. Ho, A unique sandwich structure of a CoMnP/Ni₂P/NiFe electrocatalyst for highly efficient overall water splitting, *J. Mater. Chem. A* 7 (2019) 12325–12332, <https://doi.org/10.1039/c9ta02551k>.
- [33] D. Jiang, W. Ma, R. Yang, B. Quan, D. Li, S. Meng, M. Chen, Nickel-manganese bimetallic phosphides porous nanosheet arrays as highly active bifunctional hydrogen and oxygen evolution electrocatalysts for overall water splitting, *Electrochim. Acta* 329 (2020), <https://doi.org/10.1016/j.electacta.2019.135121>.
- [34] C. Xing, F. Musharavati, H. Li, E. Zalezhad, O.K.S. Hui, S. Bae, B.Y. Cho, Synthesis, characterization, and properties of nickel-cobalt layered double hydroxide nanostructures, *RSC Adv.* 7 (2017) 38945–38950, <https://doi.org/10.1039/c7ra06670h>.
- [35] S. Kandula, K.R. Shrestha, G. Rajeshkanna, N.H. Kim, J.H. Lee, Kirkendall growth and Ostwald ripening induced hierarchical morphology of Ni-Co LDH/MMoS_x (M = Co, Ni, and Zn) heteronanostructures as advanced electrode materials for asymmetric solid-state supercapacitors, *ACS Appl. Mater. Interfaces* 11 (2019) 11555–11567, <https://doi.org/10.1021/acsaami.9b02978>.
- [36] D. Tyndall, M.J. Craig, L. Gannon, C. McGuinness, N. McEvoy, A. Roy, M. García-Melchor, M.P. Browne, V. Nicolosi, Demonstrating the source of inherent instability in NiFe LDH-based OER electrocatalysts, *J. Mater. Chem. A* (2023), <https://doi.org/10.1039/D2TA07261K>.
- [37] Q. Zhang, D. Yan, Z. Nie, X. Qiu, S. Wang, J. Yuan, D. Su, G. Wang, Z. Wu, Iron-doped NiCoP porous nanosheet arrays as a highly efficient electrocatalyst for oxygen evolution reaction, *ACS Appl. Energy Mater.* 1 (2018) 571–579, <https://doi.org/10.1021/acsaem.7b00143>.
- [38] Y. Zhang, L. Gao, E.J.M. Hensen, J.P. Hofmann, Evaluating the stability of Co₂P electrocatalysts in the hydrogen evolution reaction for both acidic and alkaline electrolytes, *ACS Energy Lett.* 3 (2018) 1360–1365, <https://doi.org/10.1021/acsaenergylett.8b00514>.
- [39] J. Ge, W. Zhang, J. Tu, T. Xia, S. Chen, G. Xie, Suppressed jahn-teller distortion in NiCo₂O₄@Ni₂P heterostructures to promote the overall water splitting, *Small* 16 (2020) 1–9, <https://doi.org/10.1002/smll.202001856>.
- [40] H. Liang, A.N. Gandhi, C. Xia, M.N. Hedhili, D.H. Anjum, U. Schwingenschlögl, H. N. Alshareef, Amorphous NiFe-OH/NiFeP electrocatalyst fabricated at low temperature for water oxidation applications, *ACS Energy Lett.* 2 (2017) 1035–1042, <https://doi.org/10.1021/acsaenergylett.7b00206>.
- [41] T. Chen, M. Qian, X. Tong, W. Liao, Y. Fu, H. Dai, Q. Yang, Nanosheet self-assembled NiCoP microflowers as efficient bifunctional catalysts (HER and OER) in alkaline medium, *Int. J. Hydrog. Energy* 46 (2021) 29889–29895, <https://doi.org/10.1016/j.ijhydene.2021.06.121>.
- [42] Y. Zhai, X. Ren, Y. Sun, D. Li, B. Wang, S. (Frank) Liu, Synergistic effect of multiple vacancies to induce lattice oxygen redox in NiFe-layered double hydroxide OER catalysts, *Appl. Catal. B Environ.* 323 (2023), 122091, <https://doi.org/10.1016/j.apcatb.2022.122091>.
- [43] H. Roh, H. Jung, H. Choi, J.W. Han, T. Park, S. Kim, K. Yong, Various metal (Fe, Mo, V, Co)-doped Ni₂P nanowire arrays as overall water splitting electrocatalysts and their applications in unassisted solar hydrogen production with STH 14%, *Appl. Catal. B Environ.* 297 (2021), 120434, <https://doi.org/10.1016/j.apcatb.2021.120434>.
- [44] D. Acharya, I. Pathak, B. Dahal, P. Chandra, R. Mangal, A. Muthurasu, T. Kim, T. Hoon, K. Chhetri, H. Yong, Immoderate nanoarchitectures of bimetallic MOF derived Ni-Fe-O/NPC on porous carbon nanofibers as freestanding electrode for asymmetric supercapacitors, *Carbon N. Y* 201 (2023) 12–23, <https://doi.org/10.1016/j.carbon.2022.08.091>.
- [45] P.P. Dhakal, U.N. Pan, D.R. Paudel, M.R. Kandel, N.H. Kim, J.H. Lee, Cobalt-manganese sulfide hybridized Fe-doped 1T-Vanadium disulfide 3D-Hierarchical core-shell nanorods for extreme low potential overall water-splitting, *Mater. Today Nano.* 20 (2022), 100272, <https://doi.org/10.1016/j.mtnano.2022.100272>.
- [46] X. Zhang, Y. Wu, Y. Sun, Q. Liu, L. Tang, J. Guo, CoFeP hollow cube as advanced electrocatalyst for water oxidation, *Inorg. Chem. Front.* 6 (2019) 604–611, <https://doi.org/10.1039/c8qi01227j>.
- [47] Z. Huang, Z. Chen, Z. Chen, C. Lv, H. Meng, C. Zhang, Ni₁₂P₅ nanoparticles as an efficient catalyst for hydrogen generation via electrolysis and photoelectrolysis, *ACS Nano* 8 (2014) 8121–8129, <https://doi.org/10.1021/nm5022204>.

- [48] Y. Bai, T.T. Nguyen, R. Chu, N.H. Kim, J.H. Lee, Core-shell hollow nanostructures as highly efficient polysulfide conversion and adsorption cathode for shuttle-free lithium-sulfur batteries, *Chem. Eng. J.* 454 (2023), 140338, <https://doi.org/10.1016/j.cej.2022.140338>.
- [49] D.-H. Park, M.-H. Kim, M. Kim, J. Byeon, J. Jang, J.-H. Kim, D. Lim, S.-H. Park, Y. Gu, J. Kim, K. Park, Spherical nickel doped cobalt phosphide as an anode catalyst for oxygen evolution reaction in alkaline media: From catalysis to system, *Appl. Catal. B Environ.* 327 (2023), 122444, <https://doi.org/10.1016/j.apcatb.2023.122444>.
- [50] M.R. Singh, K. Papadantonakis, C. Xiang, N.S. Lewis, An electrochemical engineering assessment of the operational conditions and constraints for solar-driven water-splitting systems at near-neutral pH, *Energy Environ. Sci.* 8 (2015) 2760–2767, <https://doi.org/10.1039/c5ee01721a>.
- [51] S. Piontek, C. Andronescu, A. Zaichenko, B. Konkena, K. Junge Puring, B. Marler, H. Antoni, I. Sinev, M. Muhler, D. Mollenhauer, B. Roldan Cuenya, W. Schuhmann, U.P. Apfel, Influence of the Fe:Ni ratio and reaction temperature on the efficiency of $(\text{Fe}_x\text{Ni}_{1-x})\text{S}_8$ electrocatalysts applied in the hydrogen evolution reaction, *ACS Catal.* 8 (2018) 987–996, <https://doi.org/10.1021/acscatal.7b02617>.
- [52] Y. Tang, F. Liu, W. Liu, S. Mo, X. Li, D. Yang, Y. Liu, S.-J. Bao, Multifunctional carbon-armored Ni electrocatalyst for hydrogen evolution under high current density in alkaline electrolyte solution, *Appl. Catal. B Environ.* 321 (2023), 122081, <https://doi.org/10.1016/j.apcatb.2022.122081>.
- [53] D. Yang, J.-H. Yang, Y.-P. Yang, Z.-Y. Liu, High-dispersed ruthenium sites on copper phosphide/graphene for electrocatalytic hydrogen evolution in acidic and alkaline conditions, *Appl. Catal. B Environ.* 326 (2023), 122402, <https://doi.org/10.1016/j.apcatb.2023.122402>.
- [54] W. Li, H. Zhang, K. Zhang, W. Hu, Z. Cheng, H. Chen, X. Feng, T. Peng, Z. Kou, Monodispersed ruthenium nanoparticles interfacially bonded with defective nitrogen-and-phosphorus-doped carbon nanosheets enable pH-universal hydrogen evolution reaction, *Appl. Catal. B Environ.* 306 (2022), 121095, <https://doi.org/10.1016/j.apcatb.2022.121095>.
- [55] Y. Gao, Z. Chen, Y. Zhao, W. Yu, X. Jiang, M. He, Z. Li, T. Ma, Z. Wu, L. Wang, Facile synthesis of MoP-Ru₂P on porous N, P co-doped carbon for efficiently electrocatalytic hydrogen evolution reaction in full pH range, *Appl. Catal. B Environ.* 303 (2022), 120879, <https://doi.org/10.1016/j.apcatb.2021.120879>.
- [56] Q. Yu, Y. Fu, J. Zhao, B. Li, X. Wang, X. Liu, L. Wang, Boron doping activate strong metal-support interaction for electrocatalytic hydrogen evolution reaction in full pH range, *Appl. Catal. B Environ.* 324 (2023), 122297, <https://doi.org/10.1016/j.apcatb.2022.122297>.
- [57] H. Zhang, A.W. Maijenburg, X. Li, S.L. Schweizer, R.B. Wehrspohn, Bifunctional heterostructured transition metal phosphides for efficient electrochemical water splitting, *Adv. Funct. Mater.* 30 (2020), <https://doi.org/10.1002/adfm.202003261>.
- [58] L. Yu, J. Zhang, Y. Dang, J. He, Z. Tobin, P. Kerns, Y. Dou, Y. Jiang, Y. He, S.L. Suib, In situ growth of Ni₂P-Cu₃P bimetallic phosphide with bicontinuous structure on self-supported NiCuC substrate as an efficient hydrogen evolution reaction electrocatalyst, *ACS Catal.* 9 (2019) 6919–6928, <https://doi.org/10.1021/acscatal.9b00494>.
- [59] K. Chhetri, A. Muthurasu, B. Dahal, T. Kim, T. Mukhiya, S.-H. Chae, T.H. Ko, Y. C. Choi, H.Y. Kim, Engineering the abundant heterointerfaces of integrated bimetallic sulfide-coupled 2D MOF-derived mesoporous CoS₂ nanoarray hybrids for electrocatalytic water splitting, *Mater. Today Nano* 17 (2022), 100146, <https://doi.org/10.1016/j.mtnano.2021.100146>.
- [60] M.B. Poudel, A.R. Kim, S. Ramakrishnan, N. Logeshwaran, S.K. Ramasamy, H. J. Kim, D.J. Yoo, Integrating the essence of metal organic framework-derived ZnCoTe–N–C/MoS₂ cathode and ZnCo–NPS–N–CNT as anode for high-energy density hybrid supercapacitors, *Compos. Part B* (2022), 110339, <https://doi.org/10.1016/j.compositesb.2022.110339>.
- [61] U.N. Pan, D.R. Paudel, A. Kumar Das, T.I. Singh, N.H. Kim, J.H. Lee, Ni-nanoclusters hybridized 1T–Mn–VTe₂ mesoporous nanosheets for ultra-low potential water splitting, *Appl. Catal. B Environ.* 301 (2021), 120780, <https://doi.org/10.1016/j.apcatb.2021.120780>.
- [62] K. Feng, R. Song, J. Xu, Y. Chen, C. Lu, Y. Li, W. Hofer, H. Lin, Z. Kang, J. Zhong, The S-Fe(Ni) sub-surface active sites for efficient and stable overall water splitting, *Appl. Catal. B Environ.* 325 (2023), 122365, <https://doi.org/10.1016/j.apcatb.2023.122365>.
- [63] F. Bao, E. Kemppainen, I. Dorbandt, F. Xi, R. Bors, N. Maticiu, R. Wenisch, R. Bagacki, C. Schary, U. Michalczyk, P. Bogdanoff, I. Lauermaun, R. van de Krol, R. Schlattmann, S. Calnan, Host, suppressor, and promoter—the roles of ni and fe on oxygen evolution reaction activity and stability of NiFe alloy thin films in alkaline media, *ACS Catal.* 11 (2021) 10537–10552, <https://doi.org/10.1021/acscatal.1c01190>.
- [64] N.S. Gultom, T.-S. Chen, M.Z. Silitonga, D.-H. Kuo, Overall water splitting realized by overall sputtering thin-film technology for a bifunctional MoNiFe electrode: a green technology for green hydrogen, *Appl. Catal. B Environ.* 322 (2023), 122103, <https://doi.org/10.1016/j.apcatb.2022.122103>.
- [65] Y. Li, Y. Wu, H. Hao, M. Yuan, Z. Lv, L. Xu, B. Wei, In situ unraveling surface reconstruction of Ni₃P₄@FeP nanosheet array for superior alkaline oxygen evolution reaction, *Appl. Catal. B Environ.* 305 (2022), 121033, <https://doi.org/10.1016/j.apcatb.2021.121033>.
- [66] D. Shao, P. Li, D. Wang, C. Zhao, C. Zhao, High OER performance Ni(OH)₂ with hierarchical structure, *J. Solid State Electrochem.* 23 (2019) 2051–2060, <https://doi.org/10.1007/s10008-019-04299-1>.
- [67] M. Moloudi, A. Noori, M.S. Rahmanifar, Y. Shabangoli, M.F. El-Kady, N. B. Mohamed, R.B. Kaner, M.F. Mousavi, Layered double hydroxide templated synthesis of amorphous NiCoFe as a multifunctional electrocatalyst for overall water splitting and rechargeable zinc–air batteries, *Adv. Energy Mater.* 13 (2023), 2203002, <https://doi.org/10.1002/aenm.202203002>.
- [68] Y. Xin, X. Kan, L.Y. Gan, Z. Zhang, Heterogeneous bimetallic phosphide/sulfide nanocomposite for efficient solar-energy-driven overall water splitting, *ACS Nano* 11 (2017) 10303–10312, <https://doi.org/10.1021/acsnano.7b05020>.
- [69] F. Ming, H. Liang, H. Shi, X. Xu, G. Mei, Z. Wang, MOF-derived Co-doped nickel selenide/C electrocatalysts supported on Ni foam for overall water splitting, *J. Mater. Chem. A* 4 (2016) 15148–15155, <https://doi.org/10.1039/C6TA06496E>.
- [70] X. Cao, Y. Sang, L. Wang, G. Ding, R. Yu, B. Geng, A multi-interfacial FeOOH@NiCo₂O₄ heterojunction as a highly efficient bifunctional electrocatalyst for overall water splitting, *Nanoscale* 12 (2020) 19404–19412, <https://doi.org/10.1039/d0nr05216g>.
- [71] K.M. Cole, D.W. Kirk, S.J. Thorpe, In situ raman study of amorphous and crystalline Ni-Co alloys for the alkaline oxygen evolution reaction, *J. Electrochem. Soc.* 165 (2018) J3122–J3129, <https://doi.org/10.1149/2.0131815jes>.
- [72] A.C. Garcia, T. Touzalin, C. Nieuwland, N. Perini, M.T.M. Koper, Enhancement of oxygen evolution activity of nickel oxyhydroxide by electrolyte alkali cations, *Angew. Chem.* 131 (2019) 13133–13137, <https://doi.org/10.1002/ange.201905501>.
- [73] M. Gong, H. Dai, A mini review of NiFe-based materials as highly active oxygen evolution reaction electrocatalysts, *Nano Res.* 8 (2015) 23–39, <https://doi.org/10.1007/s12274-014-0591-z>.
- [74] H.-G. Boyen, P. Ziemann, U. Wiedwald, V. Ivanova, D.M. Kolb, S. Sakong, A. Gross, A. Romanyuk, M. Büttner, P. Oelhafen, Local density of states effects at the metal-molecule interfaces in a molecular device, *Nat. Mater.* 5 (2006) 394–399, <https://doi.org/10.1038/nmat1607>.
- [75] Q. Tang, D. Jiang, Mechanism of hydrogen evolution reaction on 1T-MoS₂ from first principles, *ACS Catal.* 6 (2016) 4953–4961, <https://doi.org/10.1021/acscatal.6b01211>.
- [76] Y.-J. Tang, Y. Wang, X.-L. Wang, S.-L. Li, W. Huang, L.-Z. Dong, C.-H. Liu, Y.-F. Li, Y.-Q. Lan, Molybdenum disulfide/nitrogen-doped reduced graphene oxide nanocomposite with enlarged interlayer spacing for electrocatalytic hydrogen evolution, *Adv. Energy Mater.* 6 (2016), 1600116, <https://doi.org/10.1002/aenm.201600116>.
- [77] X. Wang, H. Huang, J. Qian, Y. Li, K. Shen, Intensified Kirkendall effect assisted construction of double-shell hollow Cu-doped CoP nanoparticles anchored by carbon arrays for water splitting, *Appl. Catal. B Environ.* 325 (2023), 122295, <https://doi.org/10.1016/j.apcatb.2022.122295>.
- [78] S. Lv, Y. Deng, Q. Liu, Z. Fu, X. Liu, M. Wang, Z. Xiao, B. Li, L. Wang, Carbon-quantum-dots-involved Fe/Co/Ni phosphide open nanotubes for high effective seawater electrocatalytic decomposition, *Appl. Catal. B Environ.* 326 (2023), 122403, <https://doi.org/10.1016/j.apcatb.2023.122403>.
- [79] M. Singh, T.T. Nguyen, M.A. P. Q.P. Ngo, D.H. Kim, N.H. Kim, J.H. Lee, Metallic metastable hybrid 1T'/1T phase triggered Co,P–SnS₂ nanosheets for high efficiency trifunctional electrocatalyst, *Small* (2023), 2206726, <https://doi.org/10.1002/smll.202206726>.
- [80] S. Singh, D.C. Nguyen, N.H. Kim, J.H. Lee, Interface engineering induced electrocatalytic behavior in core-shelled CNTs@NiP₂/NbP heterostructure for highly efficient overall water splitting, *Chem. Eng. J.* 442 (2022), 136120, <https://doi.org/10.1016/j.cej.2022.136120>.
- [81] T. Xu, D. Jiao, L. Zhang, H. Zhang, L. Zheng, D.J. Singh, J. Zhao, W. Zheng, X. Cui, Br-induced P-poor defective nickel phosphide for highly efficient overall water splitting, *Appl. Catal. B Environ.* 316 (2022), 121686, <https://doi.org/10.1016/j.apcatb.2022.121686>.
- [82] X. Zhu, D.C. Nguyen, S. Prabhakaran, D.H. Kim, N.H. Kim, J.H. Lee, Activating catalytic behavior of binary transition metal sulfide-shelled carbon nanotubes by iridium incorporation toward efficient overall water splitting, *Mater. Today Nano* 21 (2023), 100296, <https://doi.org/10.1016/j.mtnano.2022.100296>.
- [83] Y.S. Park, J. Yang, J. Lee, M.J. Jang, J. Jeong, W.-S. Choi, Y. Kim, Y. Yin, M.H. Seo, Z. Chen, S.M. Choi, Superior performance of anion exchange membrane water electrolyzer: ensemble of producing oxygen vacancies and controlling mass transfer resistance, *Appl. Catal. B Environ.* 278 (2020), 119276, <https://doi.org/10.1016/j.apcatb.2020.119276>.
- [84] A. Meena, P. Thangavel, A.S. Nissimogoudar, A. Narayan Singh, A. Jana, D. Sol Jeong, H. Im, K.S. Kim, Bifunctional oxovanadate doped cobalt carbonate for high-efficient overall water splitting in alkaline-anion-exchange-membrane water-electrolyzer, *Chem. Eng. J.* 430 (2022), 132623, <https://doi.org/10.1016/j.cej.2021.132623>.
- [85] C. Jiang, J. Yang, X. Han, H. Qi, M. Su, D. Zhao, L. Kang, X. Liu, J. Ye, J. Li, Z.-X. Guo, N. Kaltsayannis, A. Wang, J. Tang, Crystallinity-modulated Co_{2-x}V_xO₄ nanoplates for efficient electrochemical water oxidation, *ACS Catal.* 11 (2021) 14884–14891, <https://doi.org/10.1021/acscatal.1c04618>.